Development and Validation of an Active Magnetic Regenerator Refrigeration Cycle Simulation

by

John Dikeos
B.Sc., Queen's University, 2003

A Thesis Submitted in Partial Fulfillment of the Requirements for the Degree of

MASTER OF APPLIED SCIENCE

in the Department of Mechanical Engineering

Development and Validation of an Active Magnetic Regenerator Refrigeration Cycle Simulation

by

John Dikeos
B.Sc., Queen's University, 2003

Supervisory Committee:

Dr. Andrew Rowe, (Department of Mechanical Engineering)

Supervisor

Dr. David Sinton, (Department of Mechanical Engineering)

Departmental Member

Dr. Peter Oshkai, (Department of Mechanical Engineering)

Departmental Member

Supervisory Committee:

Dr. Andrew Rowe, (Department of Mechanical Engineering)

Supervisor

Dr. David Sinton, (Department of Mechanical Engineering)

Departmental Member

Dr. Peter Oshkai, (Department of Mechanical Engineering)

Departmental Member

Abstract

An alternative cycle proposed for refrigeration and gas liquefaction is active magnetic regenerator (AMR) refrigeration. This technology relies on solid materials exhibiting the magnetocaloric effect, a nearly reversible temperature change induced by a magnetic field change. AMR refrigeration devices have the potential to be more efficient than those using conventional refrigeration techniques but, for this to be realized, optimum materials, regenerator design, and cycle parameters must be determined. This work focuses on the development and validation of a transient one-dimensional finite element model of an AMR test apparatus. The results of the model are validated by comparison to room temperature experiments for varying hot heat sink temperature, system pressure, and applied heat load. To demonstrate its applicability, the model is then used to predict the performance of AMRs in situations that are either time-consuming to test experimentally or not physically possible with the current test apparatus.

Table of Contents

List of Tables

List of Figures

Nomenclature

Acronyms

AMR(s)	Active Magnetic Regenerator(s)
AMRTA	Active Magnetic Regenerator Test Apparatus
FEM	Finite Element Modeling
ICE	Internal Combustion Engine
LH_2	Liquid Hydrogen
MCE(s)	Magnetocaloric Effect(s)
PRT(s)	Platinum Resistance Thermometer(s)

Symbols

A	Area
A_d	Displacer piston surface area
A_p	Particle surface area
$A_{w,o}$	Wetted outer tubing area
B	Applied magnetic field intensity
B_{high} / B_1	Final applied magnetic field intensity
B_{low} / B_0	Initial applied magnetic field intensity
c_B	Constant-field heat capacity
c_f	Fluid/constant-density heat capacity
c_v	Constant-volume heat capacity
c_p	Constant-pressure heat capacity
c_s	Solid heat capacity
$c_{s,ref}$	Reference solid heat capacity
D	Tube diameter
D^d	Dispersion coefficient
D_h	Hydraulic diameter

D_{eq}	Equivalent spherical diameter
f_o	Effective conductivity constant
G	Mass velocity
H_e	Fluid enthalpy
h	Convection heat transfer coefficient
h_e	Specific enthalpy
h_p	Particle height
j_H	Colburn j-factor
k	Conductivity
Ks	Dimensionless solid conductivity parameter
k_{eff}	Effective conductivity
k_{static}	Static conductivity
L	Sub-domain length
l_p	Particle length
M	Mass
m	Magnetization per unit mass
$\dot{m}$	Fluid mass flow rate
NTU	Number of Transfer Units parameter
P_w	Wetted perimeter
Pe	Peclet number
Pr	Prandtl number
Q_{in}	Heat absorbed
Q_{out}	Heat rejected
$\dot{Q}_{cond}$	Rate of conductive heat transfer
$\dot{Q}_{conv}$	Rate of convective heat transfer from fluid to solid
$\dot{Q}_{load}$	Rate of heat load input
$\dot{Q}_{in}$	Rate of source term energy input

$\dot{Q}_{rad}$	Rate of radiative heat input
R	Radiative resistance
r	Radius
Re	Reynolds number
S	Total system entropy
$S_{lattice+elec}$	Lattice and electronic entropy
S_M	Magnetic entropy
s	Mass specific entropy
T	Temperature
T_0	Initial temperature
T_1	Final temperature
T_C	Cold temperature
T_H	Hot heat sink temperature
T_I	Intermediate temperature
T_∞	Temperature of surroundings
t	Time
t^*	Non-dimensionalized time
U	Internal energy
u	Mass specific internal energy
V	Volume
V_p	Particle volume
v	Velocity
$\dot{W}_{mag}$	Rate of magnetic work transfer
w_p	Particle width
$\dot{w}_{mag}$	Mass specific rate of magnetic work transfer
x	Space
x^*	Non-dimensionalized space

Greek

α	Porosity
α_o	Effective conductivity constant
ΔT_{ad}	Adiabatic temperature change due to magnetocaloric effect
ε	Emissivity
κ	Thermal capacity ratio
μ	Dynamic viscosity
μ_0	Magnetic permeability of free space
ρ	Density
σ	Stefan-Boltzmann constant
τ	Blow duration/period
Φ	Viscous energy dissipation per unit volume
ϕ	Utilization
ϕ_{ref}	Reference utilization
ϕ_s	Sphericity
ψ	Symmetry

Common Subscripts

f	Fluid
s	Solid

Acknowledgements

This project has been much more involved than I could ever have imagined when I took it on almost two years ago. The numerous stumbling blocks that I have encountered have taught me a great deal about myself; the difficulties of maintaining patience and motivation throughout such a long and challenging assignment, in a city so far away from (my other) home, are among the principal lessons.

Along the way, many people have helped me maintain my composure, and perhaps even regain it at times. Chief (no pun intended) among these individuals has been my supervisor, Andrew Rowe. I've always been impressed with his immense knowledge, insanely busy schedule, and ability to seem unbothered by my frequent unannounced visits. Thank you for putting up with my often slow progress, especially near the beginning of the project.

The tremendous support that my friends have offered has also been invaluable. I'd especially like to thank those within IESVic and the Cryofuels lab for helping to make every day a little more interesting. Among these individuals, I'd like to single out Armando Tura for being a fellow AMR researcher and frequent squash opponent, Italian language instructor, and party host. Thank you for continuing to remind me that we must strive to enjoy every moment of our lives.

I also greatly appreciate my family's unconditional support, both emotional and financial. Being thousands of kilometres away from home hasn't been easy and trips back home, where I can almost forget about the dual life I lead, have been essential in preserving my sanity. Thank you for putting up with my constant realizations that this degree was going to take yet another semester to complete.

I'd also like to acknowledge the financial support provided by NSERC. Lastly, since I see no reason to restrict the acknowledgements to people, thank you to the west coast. I have thoroughly enjoyed the mild winters, early springs, and beautiful nature that you have to offer. I promise that I will be back.

Chapter 1 – Introduction

1.1 Background

Since the beginning of the industrial revolution, society's appetite for energy services has grown exponentially. The majority of the energy requirement for these has come from carbon-based energy sources such as coal, crude oil, and natural gas. The carbon dioxide emitted as a result of burning these fuels has caused the concentration of CO_2 in the atmosphere to rise by over 30 percent in the last 200 years, to a present concentration of approximately 380 ppm [1]. This absolute concentration and its current rate of increase have been found to be unprecedented in the last 400 000 years by analyses of air trapped in the major ice caps [2]. Moreover, most energy use models predict that CO_2 concentrations will have reached levels at least twice those seen in pre-industrial years by 2100 [2]. With CO_2 being the main green house gas and a consensus among the scientific community that increases in its atmospheric concentration will likely lead to global warming and climate instability, there is a real cause for concern.

Many individuals have suggested that an eventual path away from carbon dependency and towards a "hydrogen economy" is the solution to the escalation of these problems. An important benefit of hydrogen technology is the ease with which hydrogen and electricity can be interchanged, through fuel cells and electrolysis. This will allow for hydrogen to become viable energy storage medium, storing energy from traditional and alternative energy sources until it is needed. This also makes it possible for hydrogen to be used in place of gasoline and diesel fuels for transportation applications.

Numerous issues must be resolved before the "hydrogen economy" is fully realized. For instance, since hydrogen is a gas at room temperature, its energy density is quite low. Estimates of the amount of hydrogen needed to drive 500 km with a mid-sized, fuel-cell powered vehicle are between 4 and 6 kg [3]. Hydrogen can be compressed but very high pressures are required in order to obtain reasonable volumetric densities. In fact, even the latest 70 MPa (10 000

psi) hydrogen storage tanks, which are in the process of being certified, would require over 125 L of internal volume to store 5 kg of hydrogen. This is much larger than the average 50 L fuel tank currently used by gasoline ICE vehicles [4]. In addition, compression is an inefficient and expensive process. Hydrogen can also be stored in liquid form. This is very effective since liquid hydrogen (LH_2) is almost 850 times denser than hydrogen gas at standard temperature and pressure. Only 70 L of internal volume, a size competitive with modern fuel tanks, would be required to store 5 kg of hydrogen in this manner.

Unfortunately, for hydrogen to liquefy at reasonable pressures, it must be cooled to cryogenic temperatures as low as 20 K (-253°C). With conventional cooling techniques, this means that up to 30 percent of the energy present in the liquefied product must be used in the liquefaction process [5]. Although there is the potential of recovering some of the exergy within the LH_2 as it warms up, significant cost benefits would result from increased efficiency. This has led to research being focused towards the development of more efficient and cheaper hydrogen liquefaction processes. These processes have the potential to make liquid hydrogen storage a more viable storage option for many applications, both transportation and non-transportation related.

1.2 Magnetic Refrigeration

Throughout modern history, refrigeration has typically been achieved through the use of gas-compression cycles. Although this approach is both effective and reliable, the efficiency of this type of refrigeration is limited due to significant irreversibilities in the associated compression and heat transfer processes. Magnetic refrigeration is being considered as an alternative to conventional refrigeration systems since the theoretical losses associated with it are substantially lower. In addition to higher efficiency, magnetic refrigeration systems offer potential advantages such as reduced cost and size and improved reliability.

1.2.1 The Magnetocaloric Effect

Magnetic refrigeration is based on a principle known as the magnetocaloric effect (MCE). The MCE is characterized by a temperature change that is exhibited by a magnetic material when it is subjected to a magnetic field, B. Depending on the material, this effect is largely reversible, meaning that the temperature will essentially return to its initial value if the magnetic field is removed. The MCE is a result of the alignment of the spins of the unpaired electrons, or magnetic moments, within a material when it is in the presence of a magnetic field [6]. As shown in Figure 1.1, for an adiabatic and reversible process, this alignment causes a decrease, $\Delta S_{M,ad}$, in the magnetic entropy, S_M, as the magnetic field intensity increases from B_0 to B_1. Since the total system entropy, S, must remain constant under isentropic conditions, the lattice entropy increases, causing an adiabatic temperature increase, ΔT_{ad}. When the magnetic field is removed, the magnetic entropy of the material increases and its temperature is, therefore, decreased as a result of the compensating reduction in lattice entropy.

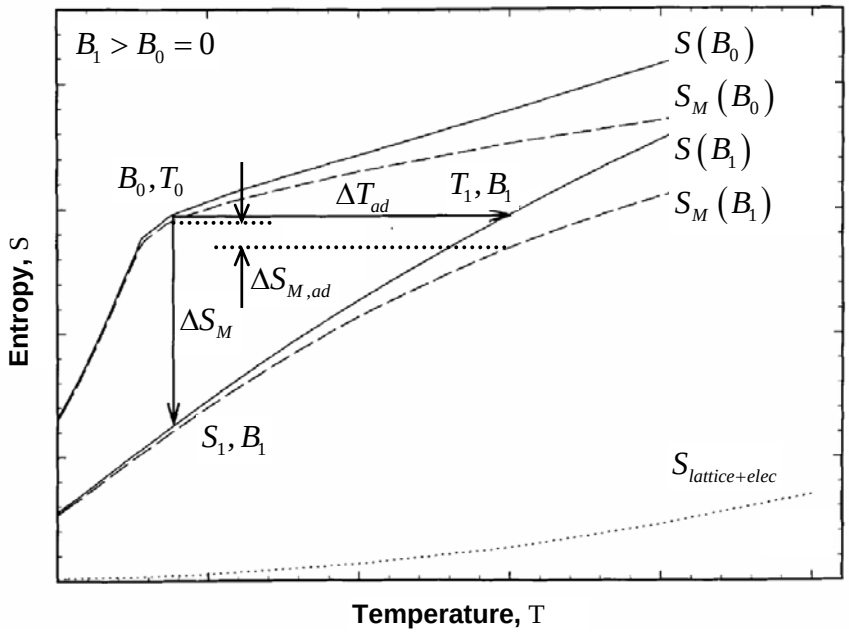

Figure 1.1 – An illustration of entropy changes associated with the MCE [7].

The MCE is generally a strong non-linear function of temperature and is largest in magnitude when a material is near its magnetic ordering temperature, also

known as the Curie temperature. This is the temperature at which long range magnetic order abruptly disappears, signalling a phase transition from ferromagnetic to paramagnetic [8]. More simply, this is the temperature at which a permanent magnet or magnetic material loses its ability to hold magnetization. The MCE is also a function of the magnitude of the magnetic field change, with the maximum MCE for most materials being on the order of 2–3 K/Tesla [9]. Gadolinium, Gd, a rare-earth metal, is the most thoroughly studied material for its MCE and the standard by which other materials are compared for room-temperature applications [6]. Figure 1.2 is derived from experimental results for the temperature increase in Gd with applied magnetic fields of 2 and 5 T. Although the 'caret'-like shape seen with Gd is the most common type of MCE behavior, "table"-like and "skyscraper"-like shapes are also possible [6].

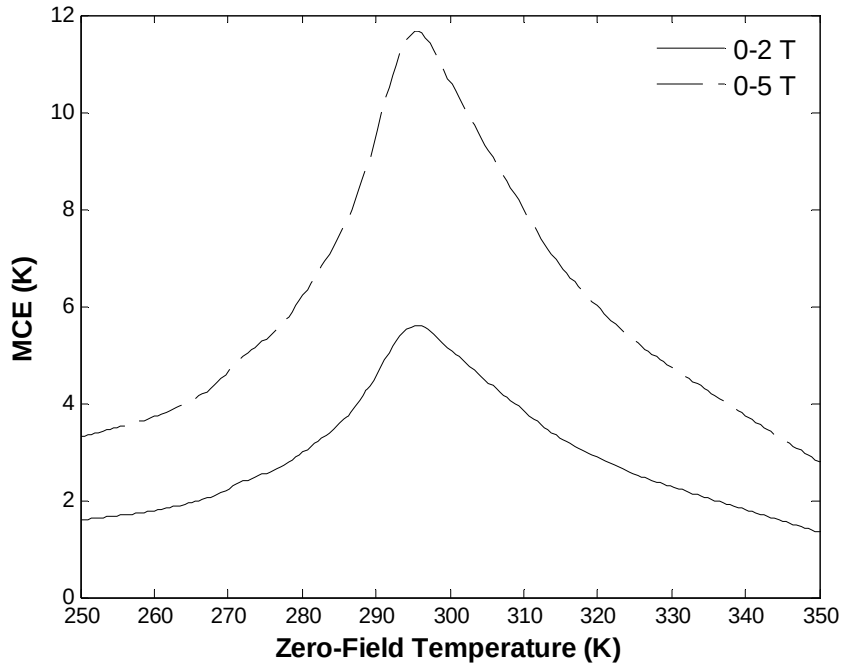

Figure 1.2 – The MCE of Gd for 0-2 T and 0-5 T field changes [10].

1.2.2 Early History

The first practical application of the MCE was a batch-cooling technique for ultra-low-temperature studies, starting in the 1930's [6]. This technique, still used today, involves cooling a magnetic material in the presence of a magnetic field and then removing the field to attain a much lower temperature than would

otherwise be possible. Although this approach is useful for attaining temperatures very close to absolute zero, it cannot be used to maintain these low temperatures since it does not include the continuous heat uptake and rejection steps of a typical refrigeration cycle.

The first magnetic refrigeration system was built for low-temperature experiments in 1953 and operated between 1 K and 0.73 K [7]. It wasn't until 1975 that a system was built that operated in the vicinity of room temperature [7]. Magnetic refrigeration was still limited, however, since the MCE is not large enough to produce temperature spans much greater than 10 K if practical magnetic field strengths are used [9]. This shortfall led to the introduction and development of the active magnetic regenerator by Steyert and Barclay, starting in 1982 [7].

1.2.3 The Active Magnetic Regenerator

A regenerator is a porous bed of material with high heat capacity that is used to transfer heat from one fluid stream to another. It differs from a heat exchanger in that it cannot continuously transfer heat and must instead be used in a cyclic manner. For example, in an application where heat must be transferred from a hot stream to a cold stream, the hot stream would first be blown through a regenerator bed. The regenerator would absorb heat from the hot stream, with the amount absorbed being dependant on factors such as the length of the blow and the heat capacities of the fluid and regenerator material. The cold stream would then be blown through the regenerator, absorbing some of the heat stored within the bed in the process. The regenerator, then, acts as a thermal buffer. Regenerators are more effective and compact than typical heat exchangers due to their extraordinarily high wetted area per unit volume, however, they are often more difficult to implement due to the cyclic nature of the fluid flow and the sometimes high pressure drops across them.

An active magnetic regenerator (AMR) introduces the concept of turning a heat exchanger, a thermodynamically passive device, into an active heat source and sink by combining conventional regenerator properties with the MCE [9]. This is

accomplished by using a magnetic material for the porous regenerator bed, making the regenerator active in the magnetic refrigeration cycle. Magnetic solids, such as Gd, are well suited for the dual role of refrigerant and heat transfer medium because they inherently have a high heat capacity near their ordering temperature, also the region in which the MCE is most predominant [6].

The most important advantage of the AMR concept, however, is the manner in which it allows temperature spans much larger than the MCE of a given material to develop. As fluid is blown through an AMR and a temperature gradient is established across it, each section of the regenerator undergoes its own unique cycle at the local temperature. The addition of all these cycles, as opposed to the uniform cycle that would be experienced by a large solid mass, accounts for the large temperature spans achievable through the use of AMRs.

1.2.4 Magnetic Refrigeration Cycle

The principle of AMR operation is often explained by approximating the operation of a system with a magnetic Brayton cycle, which consists of two adiabatic processes and two isofield processes. The procedure is summarized in the following steps and shown schematically in Figure 1.3:

1. The AMR is adiabatically magnetized, leading to an isentropic temperature rise throughout the bed (a-b).
2. Heat transfer fluid is blown through the bed from the cold end to the hot end (b-c). The heat collected is rejected through a heat exchanger at the hot sink (Q_{out}).
3. The regenerator is adiabatically demagnetized, leading to an isentropic temperature drop throughout the bed (c-d).
4. Heat transfer fluid is blown through the bed from the hot end to the cold end (d-a). The cooling power is used to absorb heat in order to refrigerate a thermal load (Q_{in}).

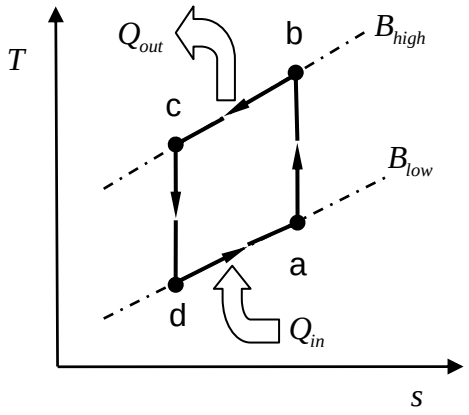

Figure 1.3 – Temperature versus entropy diagram for a magnetic Brayton cycle.

1.2.5 Multi-Layer Regenerators

As was discussed in Section 1.2.1, the MCE for a given material is largest near its Curie temperature. Figure 1.2 shows that the MCE for Gd at its magnetic ordering temperature of approximately 295 K and for a field change of 0-2 T is about 5.5 K. The MCE drops off quite quickly as one departs from this region. The confinement of large MCEs to a narrow temperature range can create problems since AMR refrigerators can operate with temperature spans in excess of 50 K. This means that a large MCE will also be localized to a small region within the regenerator, limiting the performance of the system. This limitation can be overcome through the principle of multi-layer AMRs.

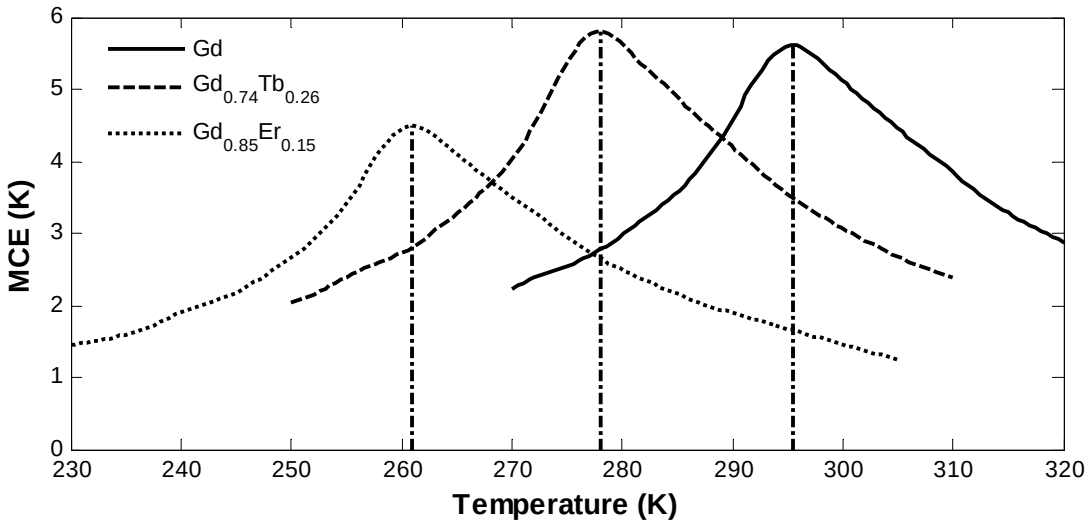

Figure 1.4 – Layering a regenerator with these materials can broaden the effective MCE curve of an AMR. The vertical dashed lines indicate the Curie temperature of each material.

Multi-layer AMRs are composed of multiple magnetocaloric materials such that each layer performs in the vicinity of its Curie temperature. As shown in Figure 1.4, this has the potential to essentially broaden the effective MCE curve. Although this concept has the potential to improve the performance of AMR refrigeration systems, special attention must be given to losses induced as a result of varying material properties at the layer boundaries and the magnetic interactions between layers. This idea is seemingly intuitive, however, it has proven difficult to validate. Also, issues such as the ideal number of materials to be used and the relative amount of each for optimum performance have yet to be addressed.

1.2.6 AMR Device Configurations

While the AMR concept is now widely used for magnetic refrigeration, the geometry, arrangement and method in which the regenerator beds interface with the magnet and heat transfer fluid subsystems can vary widely. Devices can be divided into three basic categories; reciprocating, rotary, and pulsed-field [11]. Reciprocating devices use a piston-cylinder arrangement to magnetize and demagnetize regenerators by moving them into and out of a stationary magnetic field. Rotary devices also use stationary magnetic fields, however, wheels containing AMRs are rotated into and out of magnetic fields instead. Pulsed-field designs, on the other hand, use stationary regenerators and vary the intensity of the magnetic fields. This is generally accomplished through the use of electromagnets but configurations utilizing rotating permanent magnets have also been conceived. Each of the configurations mentioned has its advantages and disadvantages. Reciprocating systems are reliable and relatively simple to implement but they can be bulky and have large inertial forces that limit both operating frequency and mechanical efficiency. Rotary devices can be more efficient, smaller, and better at balancing magnetic and inertial forces, yet they are more complex and often present difficult sealing problems. Lastly, pulsed-field systems frequently require little or no mechanical movement and can be very space-efficient but it is quite difficult to pulse electromagnets at the

frequencies required and the losses associated with this process can be quite high.

1.2.7 Active Magnetic Regenerator Test Apparatus

The Active Magnetic Regenerator Test Apparatus (AMRTA) designed and constructed by the Cryofuels group at the University of Victoria is of the reciprocating type [11]. This design was chosen for the flexibility it offers in allowing for the effects of a broad array of parameters to easily be varied and tested. For instance, AMRs of different lengths, cross-sectional areas, and compositions can easily be swapped and parameters such as system pressure and operating frequency can easily be adjusted. Although the disadvantages of this configuration mentioned earlier would not make it a likely candidate for commercial application, it is ideal for experimental analysis.

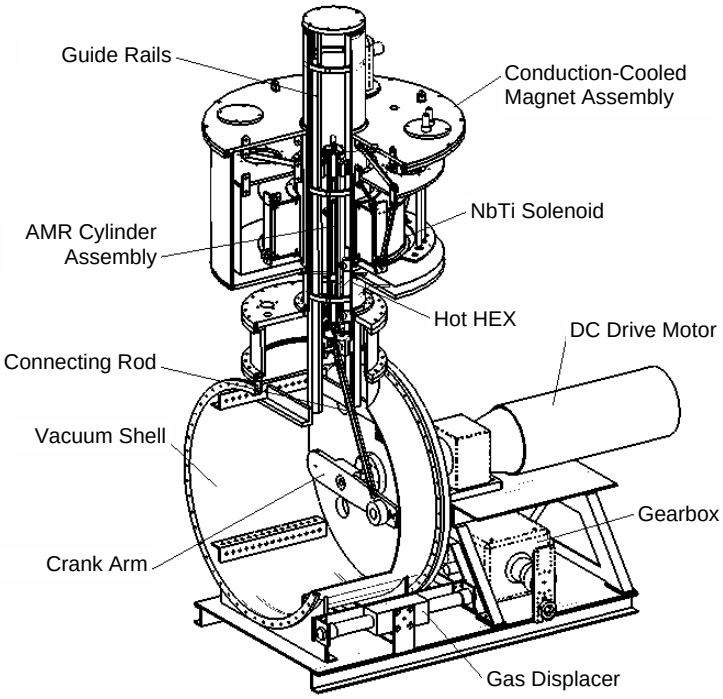

Figure 1.5 – A partly cut-away schematic illustration of the AMRTA [11].

The AMRTA, shown schematically in Figure 1.5, is composed of a cylindrical superconducting magnet, a composite cylinder housing two regenerators, and a piston-cylinder arrangement that is used to drive this cylinder, and hence the regenerators, into and out of the magnetic field produced by the magnet. As

shown in Figure 1.6, the AMRs in the cylinder are set a distance apart from each other so that they are nearly 180^{o} apart in terms of the magnetic field applied to them. This implies that while one regenerator is being subjected to the maximum intensity field in the center of the magnet, the other is at its furthest distance away from the center of the magnet and is, therefore, subject to the minimum possible magnetic field intensity. Using two regenerators in this way essentially doubles the cooling power of the system, resulting in more effective low frequency operation. This also allows for a cold section to be created between the regenerators. Resistive elements just below the AMRs are then used to mimic the application of a particular cooling load. The movement of the cylinder containing the AMRs occurs along guide rails with the aid of oil-impregnated bushings. This movement is coupled to a displacer that acts to pulse the flow through the regenerators in alternating directions. Helium is used as the heat transfer fluid in this device. The cylinder and crank mechanism are housed within an evacuated chamber in an attempt to reduce the magnitude of heat leaks into the system.

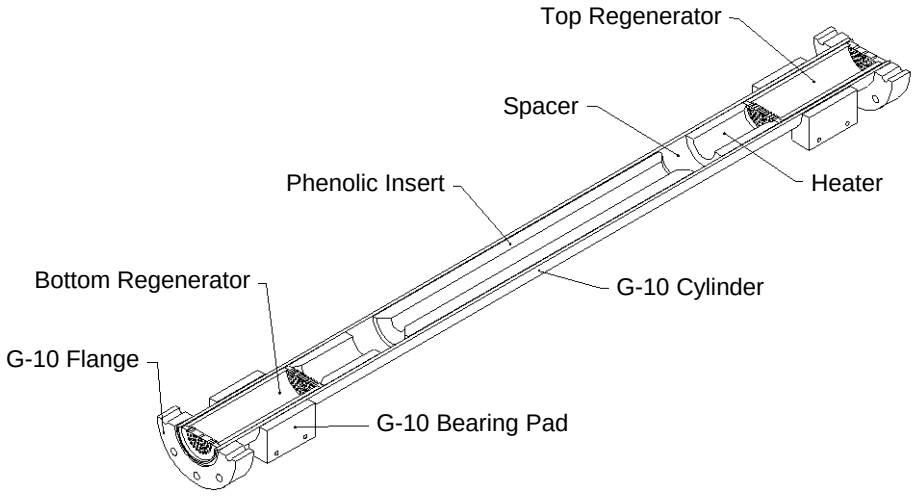

Figure 1.6 – A cross-sectional view of the AMRTA cylinder [11].

Figure 1.7 depicts a schematic of the AMR test apparatus which is useful in visualizing how the major components interact with each other. Two layered regenerators are shown on either end of the cylinder. The magnet, which moves with respect to the cylinder in order to periodically magnetize each of the AMRs,

is also shown. The displacer on the bottom is responsible for the periodic fluid flow, while the heat exchangers on either end represent the hot heat sinks. A simplified temperature profile through the cylinder is also shown. Electric heaters are placed in the cold section created between the two AMRs. As mentioned earlier, these components are employed to simulate the operation of the test apparatus with set values of cooling power.

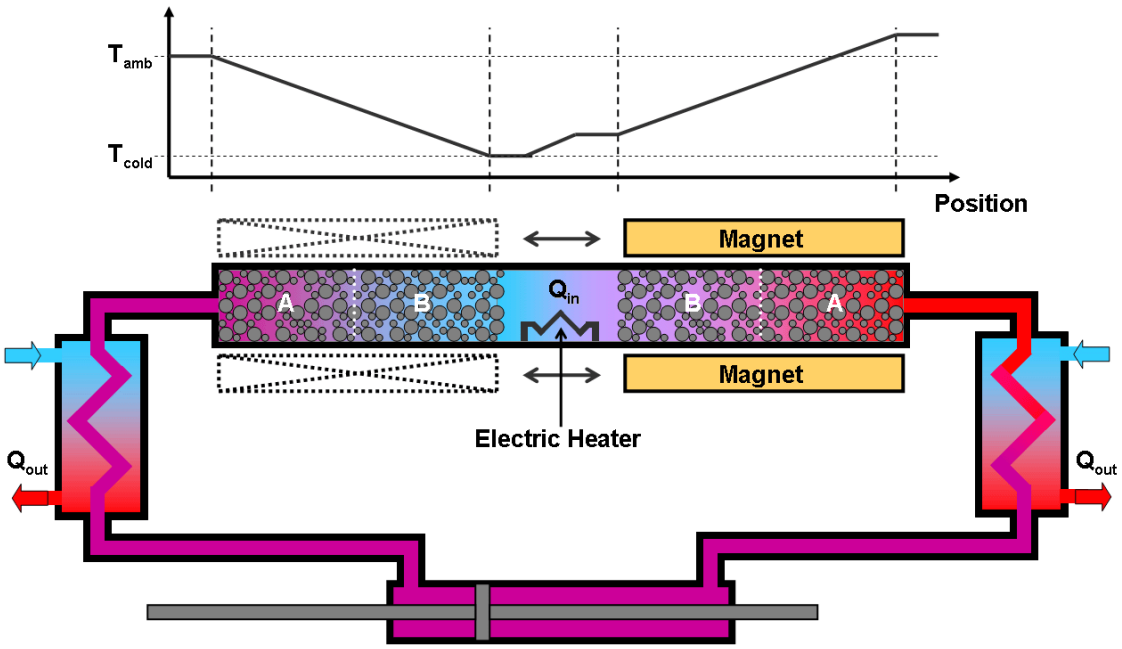

Figure 1.7 – A schematic of the AMR test apparatus showing a simplified temperature variation through the cylinder [12].

1.3 Objective

A great deal of research must be conducted before AMR refrigeration becomes commercially viable, either for room temperature refrigeration applications or for the liquefaction of natural gas and hydrogen. This research will help address the optimization of parameters such as system mass flow rate and frequency, and AMR shape, aspect ratio, and material composition.

The purpose of this work is to develop a model that can accurately simulate the operation of the AMRTA, allowing for a parallel program of research through numerical simulation and experimentation to occur. Simulations can have many advantages over experiments, beyond their obvious potential to improve overall

system understanding. For instance, simulation results can be obtained relatively quickly and cheaply, with no risk of component damage. Simulations can also be used to conduct in-depth parametric investigations. One area where simulations can be particularly useful is with the optimization of multi-layer AMRs. Varying the amount of each material experimentally would be a time-consuming task but this operation involves just a slight adjustment of a few variables in the case of a system model. Another objective of this work is to extensively validate the numerical simulation with experimental results. This is necessary to guarantee the accuracy of the model.

Chapter 2 provides some background information on AMR modeling, outlining some of the key features of the model developed here and comparing it to others that have been developed in the past. The following chapter outlines the derivation of the governing equations that are used to describe the flow of energy throughout the system. Next, it is necessary to describe how the various required properties are obtained or calculated. This leads to a description of the method by which the model is implemented into a finite element modeling package and validated through direct comparison with experimental data. The results of this validation procedure and the results of some predictive simulations are then presented and discussed. Lastly, conclusions and recommendations are made to highlight the degree to which the model development is successful and suggest future work that can be done to improve upon it.

Chapter 2 – Model Background and Description

The purpose of this chapter is to provide background information on AMR modeling and outline the assumptions used in the development of this numerical simulation.

2.1 Comparison with Previous Works

Several attempts have been made to model AMR refrigeration systems in the past [11, 13-17]. To reduce computational time, simulations of this type are generally one-dimensional analyses. Further, except for the models developed by Rowe [11] and Spearing [13], the model domain of other simulations encompasses only one AMR. In this case, two boundary conditions must be specified; those at the hot and cold ends. This artificially imposes a temperature span across the AMR which relates to a particular cooling power that can be calculated. These other simulations also typically approximate the operation of an AMR refrigerator with a simplified model such as a magnetic Brayton cycle. Stepping and ramping functions, which are often unrealistic and possible causes of numerical instability, are typically used to model the application of fluid blow and magnetization in these situations. Furthermore, some models make simplifications to reduce computational time. These include neglecting axial conductivity, dispersion effects, and void space thermal mass, and assuming properties such as the regenerator and fluid heat capacities are constant. Lastly, none of the previous works have been thoroughly validated with experimental results from a magnetic refrigeration apparatus.

Although the model presented in this thesis is also based on a one-dimensional analysis, it differs from previous work in several ways. For instance, the model domain encompasses two AMRs and a cold space between them. This setup mimics the operation of a magnetic refrigeration apparatus since it requires only the hot heat sink boundary temperature and allows for a temperature span to develop across each of the regenerators based on the magnitude of heat absorbed in the cold section. Further, a realistic model of the magnetic

refrigeration cycle with magnetic field and mass flow rate variations occurring simultaneously and varying in a sinusoidal manner is implemented in this work. In an attempt to model the AMR test apparatus accurately, few simplifications are made in the derivation and application of the governing equations. The most important difference between this work and previous models, though, is the existence of experimental data with which to confirm its accuracy. This resource has proven to be invaluable and will, no doubt, continue to do so.

2.2 Assumptions

Several assumptions are made in order to simplify the analysis and application of the governing equations. These assumptions, justified in the following text, are:

- A one-dimensional analysis is sufficiently representative. This assumes a fully-developed flow, negligible heat leaks, and infinite thermal conduction in the transverse direction.
- The regenerator matrix is homogeneous, stationary, and has a uniform porosity and cross-sectional area.
- The mass flow rate across the domain is constant, as is the amount of fluid entrained in the matrix and cold section.
- Viscous dissipation throughout the model domain is negligible.
- The magnetic field intensity which each of the regenerators is subjected to is constant across each of them and eddy-current dissipation is negligible.

A one-dimensional flow assumption is common in thermal regenerator modeling and yields relatively accurate results while greatly reducing the amount of computation required. Assuming uniformity throughout each of the regenerators is also reasonable if sufficiently representative average properties can be obtained for the analysis. The assumption of uniform mass flow rate across the domain assumes that the fluid is incompressible. This claim is sensible for low velocity flows that have relatively small variations in temperature. Viscous dissipation is a result of fluid pressure drop across regenerators. It is often

neglected in passive regenerator models since regenerators are designed to minimize the pressure drop across them. An order of magnitude analysis based upon the dimensions, operating conditions, and observed pressure drop in the experimental data suggests this is a good assumption for the cases studied here. The magnetic field applied to each of the regenerators at each point in time can be assumed to be constant since the length of each of the AMRs is small compared to the sweep length of the entire cylinder. Lastly, eddy-current dissipation is not accounted for since its effects are typically negligible in regenerators. This is a result of minimized current loops due to the point contacts between particles and small particle size.

2.3 Model Domain

The model domain is intended to represent the AMRTA cylinder in its entirety, as shown in Figure 1.6. As such, it is composed of three distinct sub-domains. Two of these represent AMR beds while a third, central sub-domain is used to model the area between the regenerators. A heat source can be added to this region to simulate a cooling load. Figure 2.1 shows the one-dimensional model domain that is used to represent the cylinder. In the case of multi-layer AMRs, each of the regenerator domains is split into additional sub-domains so that each layer can be represented accordingly.

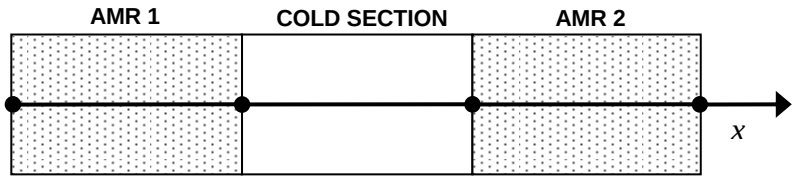

Figure 2.1 – The one-dimensional model domain used to represent the AMRTA cylinder**.**

2.4 Mass Flow Rate and Magnetic Field Variation

Although the magnetic Brayton cycle, discussed in Section 1.2.4, is helpful in explaining the concept behind magnetic refrigeration, it does not properly describe the operation of the AMRTA since the cycle steps overlap in this apparatus.

Figure 2.2 depicts a sinusoidal representation of the variation of magnetic field and fluid flow throughout an AMR cycle for a magnetic field variation of 0-2 T. This is a much more accurate model of the variation in these properties in the AMRTA. As will be shown in the development of the governing equations in Chapter 3, time is non-dimensionalized using the length of each blow, and so, one unit of non-dimensionalized time represents the duration of each blow and two units the duration of a cycle. Also, a positive mass flow rate indicates fluid flow in the positive x direction and vice-versa. Although this model of the AMR cycle is quite different from the magnetic Brayton cycle, it is important to note that the maximum flow does still occur while each of the regenerators is being subjected to either a zero or full-intensity magnetic field. If necessary, an offset may be applied to account for phase differences between the fluid flow and the applied field.

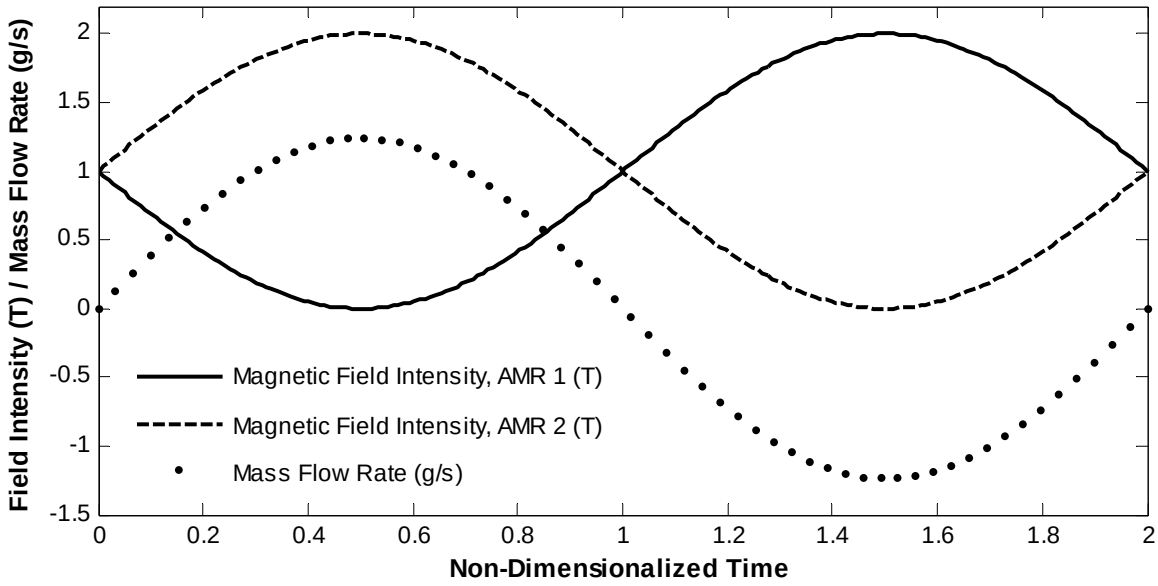

Figure 2.2 – A sinusoidal approximation of the variation of magnetic field intensity and mass flow rate in a dual-AMR, reciprocating AMR refrigeration apparatus.

Chapter 3 – Development of Governing Equations

Since the physics occurring within the two AMR sections is identical, only two sets of governing equations need to be developed to characterize the fluid flow and heat transfer throughout the model domain; one set for the AMR sections and another for the cold section between them. These equations are obtained by performing energy balances across differential segments in the direction of the fluid flow. Since the analysis of both of the sections is similar, a set of general form expressions is developed so that the individual section equations can then be derived.

3.1 General Form Equations

The simplest method of developing the energy balance equations for the AMR and cold sections is to first develop general equations. These individual equations can then be simplified to ensure that they appropriately describe the conditions within each of the sections. Combined, these expressions are used to describe the flow of energy throughout the entire model domain.

3.1.1 Fluid Energy Balance

The energy balance for a heat transfer fluid flowing through an enclosure, whether it be empty or filled with some type of porous media, can be summarized by the following:

$$\begin{matrix}\textit{RATE OF CHANGE}\\ \textit{OF ENERGY}\end{matrix} = \begin{matrix}\textit{ENTHALPY}\\ \textit{FLUX}\end{matrix} + \begin{matrix}\textit{CONDUCTIVE}\\ \textit{INPUT}\end{matrix} + \begin{matrix}\textit{CONVECTIVE}\\ \textit{INPUT}\end{matrix} + \begin{matrix}\textit{HEAT LOAD}\\ \textit{INPUT}\end{matrix} + \begin{matrix}\textit{VISCOUS}\\ \textit{DISSIPATION}\end{matrix} \qquad (3.1)$$

The enthalpy flux is due to fluid flow through an open system, while the conductive input represents conduction along the temperature gradient within the fluid. Further, energy transfer with the solid occurs due to heat transfer through convection and the viscous dissipation term denotes energy loss within the fluid flow. The heat load input term is essentially a source term, used to represent energy flows due to internal heat generation, externally applied heat loads, and work performed by or on the system. Referring to Figure 3.1 and subtracting the input from the output to determine the change, the energy balance becomes:

$$\frac{\partial U_f}{\partial t} = -\frac{\partial \dot{H}_e}{\partial x}dx - \frac{\partial \dot{Q}_{cond,f}}{\partial x}dx + \dot{Q}_{conv,s-f} + \frac{\dot{Q}_{in}}{L}dx + \Phi A_f dx \tag{3.2}$$

where, U_f is the internal energy of the fluid, $\dot{H}_e$ is the enthalpy flux of the fluid, $\dot{Q}_{cond,f}$ is the rate of conductive heat transfer within the fluid, $\dot{Q}_{conv,s-f}$ is the rate of convective heat transfer from the solid to the fluid, $\dot{Q}_{in}$ is the rate of source term input, L is the total length of the sub-domain, Φ represents the viscous energy dissipation per unit volume, and A_f is the area of fluid flow, also known as the free-flow area.

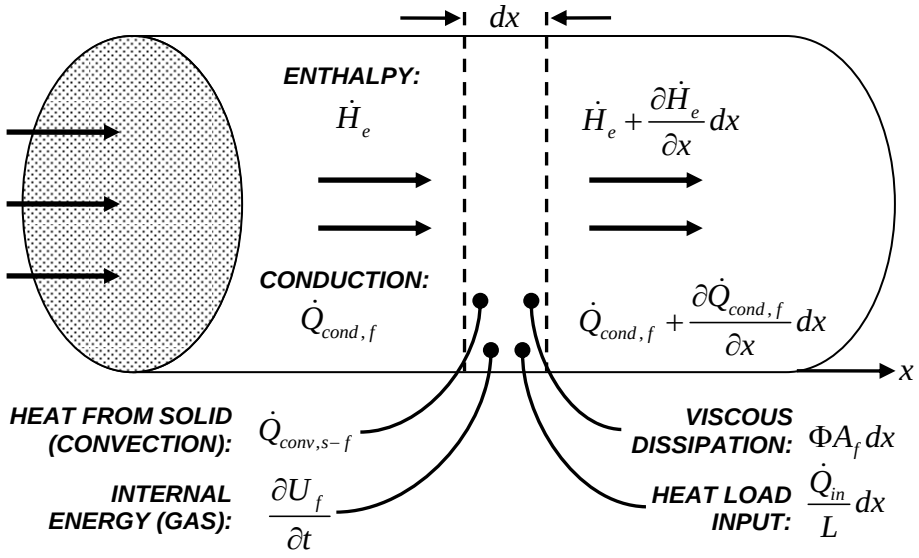

Figure 3.1 – The energy balance for the heat transfer fluid across a differential segment of the model domain.

The following relations can be used to expand the fluid energy balance equation:

$$\begin{aligned} dU_f &= M_f du_f = \left(\rho_f A_f dx\right)\left(c_v dT_f\right) \\ d\dot{H}_e &= \dot{m} dh_e = \dot{m} c_p dT_f \\ \dot{Q}_{cond,f} &= -k_f A_f \frac{\partial T_f}{\partial x} \\ \dot{Q}_{conv,s-f} &= hP_w dx\left(T_s - T_f\right) \end{aligned} \tag{3.3}$$

where, M_f is the mass of the fluid within the differential control volume, u_f is the mass specific internal energy, ρ_f is the density of the fluid, c_v and c_p are the constant-volume and constant-pressure specific heats of the fluid, T_f is the temperature of the fluid, $\dot{m}$ is the fluid mass-flow rate, h_e is the specific enthalpy, k_f is the fluid conductivity, h is the convection heat transfer coefficient, P_w is the wetted perimeter, or the total perimeter in which the fluid and solid interact for a given cross-section, and T_s is the solid or regenerator temperature. Substituting these expressions into the fluid energy balance equation and dividing through by $A_f dx$,

$$\rho_f c_v \frac{\partial T_f}{\partial t} = -\frac{\dot{m} c_p}{A_f}\frac{\partial T_f}{\partial x} + \frac{\partial}{\partial x}\left(k_f \frac{\partial T_f}{\partial x}\right) + \frac{hP_w}{A_f}\left(T_s - T_f\right) + \frac{\dot{Q}_{in}}{A_f L} + \Phi \tag{3.4}$$

It should be noted that the conductivity term is not removed from the brackets since it can vary spatially. Further, as mentioned in the assumptions in Section 2.2, viscous dissipation is neglected in this analysis, and so, this term is dropped to simplify the fluid energy balance equation. The incompressibility assumption is also helpful since the constant volume and constant pressure heat capacities are equal in this case. Thus, from this point forward, the symbol c_f will be used to represent the constant-density heat capacity of the fluid. Applying these changes to the fluid energy balance equation yields:

$$\rho_f c_f \frac{\partial T_f}{\partial t} = -\frac{\dot{m} c_f}{A_f}\frac{\partial T_f}{\partial x} + \frac{\partial}{\partial x}\left(k_f \frac{\partial T_f}{\partial x}\right) + \frac{hP_w}{A_f}\left(T_s - T_f\right) + \frac{\dot{Q}_{in}}{A_f L} \tag{3.5}$$

The wetted perimeter term can be eliminated through the use of the following relations:

$$A_f = \frac{V_f}{L}; P_w = \frac{A_w}{L}$$
$$\therefore \frac{P_w}{A_f} = \frac{A_w}{V_f} \tag{3.6}$$

where, V_f is the volume of fluid within the enclosure, or within the porous matrix in the case of the AMR sections, and A_w is the wetted area, or the total area that the heat transfer fluid and solid come in contact. Also, in order to simplify the analysis and application of the model, the time and space variables, t and x, are non-dimensionalized through the use of the following definitions:

$$t^* \equiv \frac{t}{\tau}; \quad x^* \equiv \frac{x}{L} \tag{3.7}$$

where, τ is the duration of each blow, and t^* and x^* are the non-dimensionalized units of time and space, respectively. Substituting these quantities into Equation (3.5) and multiplying through by τ / ρ_f yields:

$$c_f \frac{\partial T_f}{\partial t^*} = -\frac{\dot{m} c_f \tau}{\rho_f A_f L} \frac{\partial T_f}{\partial x^*} + \frac{\partial}{\partial x^*}\left(\frac{k_f \tau}{\rho_f L^2} \frac{\partial T_f}{\partial x^*} \right) + \frac{h A_w \tau}{\rho_f V_f}\left(T_s - T_f \right) + \frac{\dot{Q}_{in} \tau}{\rho_f A_f L} \tag{3.8}$$

This relation can be simplified further by recognizing that:

$$M_f = \rho_f V_f = \rho_f A_f L \tag{3.9}$$

where, M_f is the mass of the fluid in the regenerator matrix. Manipulating the equation further by multiplying through by $M_f / \left(M_s c_s \right)$,

$$\frac{M_f c_f}{M_s c_s} \frac{\partial T_f}{\partial t^*} = -\frac{\dot{m} c_f \tau}{M_s c_s} \frac{\partial T_f}{\partial x^*} + \frac{1}{c_s} \frac{\partial}{\partial x^*}\left(\frac{k_f A_f}{L} \frac{\tau}{M_s} \frac{\partial T_f}{\partial x^*} \right) + h A_w \frac{\tau}{M_s c_s}\left(T_s - T_f \right) + \frac{\dot{Q}_{in} \tau}{M_s c_s} \tag{3.10}$$

where, M_s is the total mass of the solid material and c_s is its heat capacity. Solid properties are introduced since the fluid and solid equations are coupled and

their use is important in grouping the coefficients of each of the terms into recognizable expressions. It should be noted, however, that the solid heat capacity is kept outside the brackets of the conduction term since this term may vary spatially. This term is manipulated by multiplying it by $c_{s,ref} / c_{s,ref}$:

$$\frac{M_f c_f}{M_s c_s}\frac{\partial T_f}{\partial t^*} = -\frac{\dot{m}c_f \tau}{M_s c_s}\frac{\partial T_f}{\partial x^*} + \frac{c_{s,ref}}{c_s}\frac{\partial}{\partial x^*}\left(\frac{k_f A_f}{L}\frac{\tau}{M_s c_{s,ref}}\frac{\partial T_f}{\partial x^*}\right) + hA_w \frac{\tau}{M_s c_s}\left(T_s - T_f\right) + \frac{\dot{Q}_{in}\tau}{M_s c_s} \tag{3.11}$$

where, $c_{s,ref}$ represents a reference solid heat capacity. In the AMR sections, for instance, the peak Curie temperature heat capacity could be used for this parameter. Multiplying the conduction and convection terms of Equation (3.11) by $\left(\dot{m}c_f\right)/\left(\dot{m}c_f\right)$ yields:

$$\frac{M_f c_f}{M_s c_s}\frac{\partial T_f}{\partial t^*} = -\frac{\dot{m}c_f \tau}{M_s c_s}\frac{\partial T_f}{\partial x^*} + \frac{c_{s,ref}}{c_s}\frac{\partial}{\partial x^*}\left(\frac{k_f A_f}{\dot{m}c_f L}\frac{\dot{m}c_f \tau}{M_s c_{s,ref}}\frac{\partial T_f}{\partial x^*}\right) + \frac{hA_w}{\dot{m}c_f}\frac{\dot{m}c_f \tau}{M_s c_s}\left(T_s - T_f\right) + \frac{\dot{Q}_{in}\tau}{M_s c_s} \tag{3.12}$$

A number of dimensionless parameters are now introduced to simplify the fluid energy balance equation further:

$$NTU \equiv \frac{hA_w}{\dot{m}c_f} \tag{3.13}$$

$$\phi \equiv \frac{\dot{m}c_f \tau}{M_s c_s} \tag{3.14}$$

$$\phi_{ref} \equiv \frac{\dot{m}c_f \tau}{M_s c_{s,ref}} \tag{3.15}$$

$$\kappa \equiv \frac{M_f c_f}{M_s c_s} \tag{3.16}$$

$$\mathrm{Pe}_f \equiv \frac{\dot{m} c_f L}{k_f A_f} \tag{3.17}$$

$$\psi \equiv \frac{c_{s,ref}}{c_s} \tag{3.18}$$

These parameters are most relevant to the regenerator sections but they are also applicable to the cold section analysis. The NTU, or Number of Transfer Units, parameter is a well-known grouping that is a measure of effectiveness of a heat exchanger. The parameters defined by Equations (3.14) through (3.16) are thermal capacity ratios; ϕ, also known as the utilization, is the ratio of fluid flow thermal capacity to solid thermal capacity, while κ is the ratio of solid thermal capacity to void space fluid thermal capacity. The alternate utilization definition is required due to the presence of the reference heat capacity in the conduction term. The next parameter, Pe_f, is a form of the Peclet number. It relates energy transfer through advection to that through heat conduction. Lastly, ψ, a parameter known as symmetry, is the ratio of the reference solid heat capacity to the spatially-varying solid heat capacity. Rearranging Equation (3.8) and substituting the dimensionless parameters defined above yields the final form of the general form heat transfer fluid energy balance equation:

$$\kappa \frac{\partial T_f}{\partial t^*} = -\phi \frac{\partial T_f}{\partial x^*} + \psi \frac{\partial}{\partial x^*}\left(\frac{\phi_{ref}}{\mathrm{Pe}_f} \frac{\partial T_f}{\partial x^*} \right) + NTU\,\phi (T_s - T_f) + \frac{\dot{Q}_{in}\tau}{M_s c_s} \tag{3.19}$$

This form of the heat transfer fluid energy balance is powerful since few simplifications are used in its derivation. The transient and diffusion terms are often neglected to yield a simplified, less computationally intensive version of this energy balance that is sufficiently representative in many cases.

3.1.2 Solid Energy Balance

In the AMR sections, the tubing is neglected and the solid is represented by the porous regenerator matrix. In contrast, the tubing is considered to be the solid in the cold section analysis. Although these cases appear to be quite different, similar expressions can be used to account for energy transfer in both situations. The energy balance for a section of AMR or tubing with heat transfer fluid flowing through it can be summarized by the following:

$$\begin{matrix}\textit{RATE OF CHANGE}\\ \textit{OF ENERGY}\end{matrix} = \begin{matrix}\textit{CONDUCTIVE}\\ \textit{INPUT}\end{matrix} + \begin{matrix}\textit{CONVECTIVE}\\ \textit{INPUT}\end{matrix} + \begin{matrix}\textit{HEAT LOAD}\\ \textit{INPUT}\end{matrix} \tag{3.20}$$

This relation is somewhat similar to the energy balance seen for the heat transfer fluid but the enthalpy and viscous dissipation terms are not present. Referring to Figure 3.2, the energy balance becomes:

$$\frac{\partial U_s}{\partial t} = -\frac{\partial \dot{Q}_{cond,s}}{\partial x}dx + \dot{Q}_{conv,f-s} + \frac{\dot{Q}_{in}}{L}dx \tag{3.21}$$

where, U_s is the internal energy of the solid, $\dot{Q}_{cond,s}$ is the rate of conductive heat transfer within the solid in the x-direction, $\dot{Q}_{conv,f-s}$ is the rate of convective heat transfer from the fluid to the solid, and $\dot{Q}_{in}$ is once again used as a source term, to represent work and heat transfer to or from the system.

The terms of Equation (3.21) can be expanded using the following relations:

$$\begin{aligned} dU_s &= M_s du_s = \left(\rho_s A_s dx\right)\left(c_s dT_s\right) \\ \dot{Q}_{cond,s} &= -k_s A_s \frac{\partial T_s}{\partial x} \\ \dot{Q}_{conv,f-s} &= hP_w dx\left(T_f - T_s\right) \end{aligned} \tag{3.22}$$

where, M_s is the mass of the solid, u_s is the specific (per unit mass) internal energy, ρ_s is the solid density, A_s is the area of solid material for a given cross-section, and k_s is the solid conductivity. Substituting these relations into the solid energy balance equation,

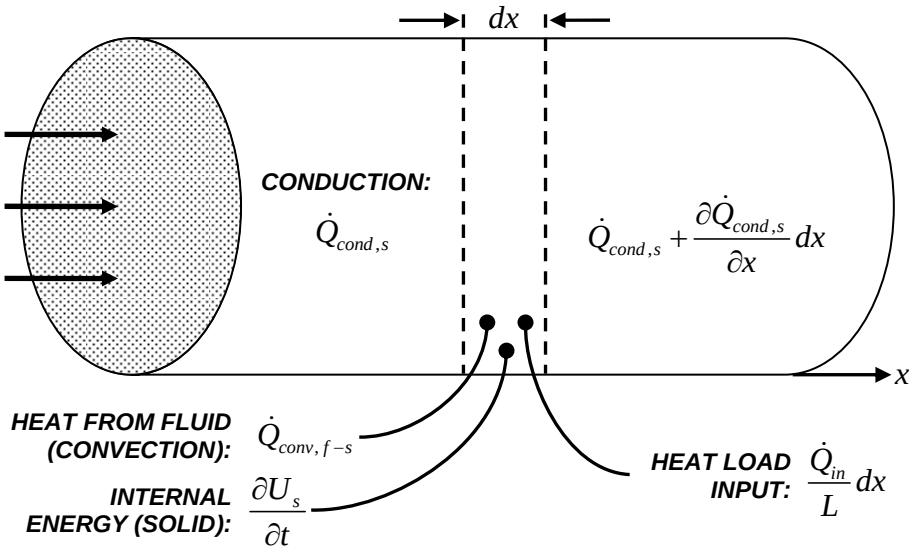

Figure 3.2 - The energy transfer for a differential segment of a solid with heat transfer fluid flowing through it.

$$\rho_s A_s c_s dx \frac{\partial T_s}{\partial t} = \frac{\partial}{\partial x}\left(k_s A_s dx \frac{\partial T_s}{\partial x} \right) + hP_w dx \left(T_f - T_s \right) + \frac{\dot{Q}_{in}}{L} dx \tag{3.23}$$

Applying Equations (3.6) and (3.7) to eliminate the wetted perimeter term, P_w, and impose non-dimensionalized units of time and space, and rearranging in order to solve for the partial derivative of the solid temperature yields:

$$\frac{\partial T_s}{\partial t^*} = \frac{1}{c_s} \frac{\partial}{\partial x^*}\left(\frac{k_s \tau}{\rho_s L^2} \frac{\partial T_s}{\partial x^*} \right) + \frac{hA_w \tau}{\rho_s A_s L c_s} \left(T_f - T_s \right) + \frac{\dot{Q}_{in} \tau}{\rho_s A_s L c_s} \tag{3.24}$$

The solid heat capacity is left outside the conduction term brackets once again since it may be spatially varying. This relation can be simplified further by recognizing that:

$$M_s = \rho_s V_s = \rho_s A_s L \tag{3.25}$$

where, M_s is the mass of the solid, whether it be the porous regenerator matrix or the tubing. Applying this expression and multiplying the conduction term by $c_{s,ref} / c_{s,ref}$ gives:

$$\frac{\partial T_s}{\partial t^*} = \frac{c_{s,ref}}{c_s}\frac{\partial}{\partial x^*}\left(\frac{k_s A_s \tau}{M_s c_{s,ref} L}\frac{\partial T_s}{\partial x^*}\right) + \frac{hA_w \tau}{M_s c_s}\left(T_f - T_s\right) + \frac{\dot{Q}_{in}\tau}{M_s c_s} \tag{3.26}$$

The coefficient in the convection term can be simplified using the dimensionless parameters defined by Equations (3.13) and (3.14) since,

$$NTU\,\phi = \frac{hA_w}{\dot{m}c_f}\frac{\dot{m}c_f \tau}{M_s c_s} = \frac{hA_w \tau}{M_s c_s} \tag{3.27}$$

Further, a new dimensionless parameter can be defined to account for the diffusion term:

$$\mathrm{Ks} \equiv \frac{M_s c_{s,ref} L}{k_s A_s \tau} \tag{3.28}$$

Substituting these quantities into the solid energy balance equation derived thus far and using the symmetry definition given by Equation (3.18) yields the final form of the general solid energy balance equation:

$$\frac{\partial T_s}{\partial t^*} = \psi\frac{\partial}{\partial x^*}\left(\frac{1}{\mathrm{Ks}}\frac{\partial T_s}{\partial x^*}\right) + NTU\,\phi(T_f - T_s) + \frac{\dot{Q}_{in}\tau}{M_s c_s} \tag{3.29}$$

3.2 Active Magnetic Regenerator Sections

The governing equations for the AMR sections describe the flow of energy as a heat transfer fluid flows through a regenerator, a porous bed composed of flakes of magnetocaloric material. The MCE must also be considered since the field applied to the AMRs changes simultaneously. These expressions are based on the general form equations derived in Section 3.1.

3.2.1 Fluid Energy Balance

In the AMR sections, the heat transfer fluid flows through regenerators. The general form heat transfer fluid energy balance expression, given by Equation (3.19), can be used to represent the flow of energy in this situation if the source term is neglected:

$$\kappa \frac{\partial T_f}{\partial t^*} = -\phi \frac{\partial T_f}{\partial x^*} + \psi \frac{\partial}{\partial x^*}\left(\frac{\phi_{ref}}{\mathrm{Pe}_f} \frac{\partial T_f}{\partial x^*} \right) + NTU\,\phi (T_s - T_f) \tag{3.30}$$

However, there is also another important modification to this expression. An effective conductivity, k_{eff}, must be used in place of the fluid conductivity embedded within the Pe_f definition of Equation (3.17). The effective conductivity represents the combined conductivity of the regenerator and fluid, taking into account dispersion effects. The use of the effective conductivity parameter is justified and explained further in Section 4.1.1. The alternate definition of the fluid Peclet number, Pe_f, for the AMR sections becomes:

$$\mathrm{Pe}_f \equiv \frac{\dot{m} c_f L}{k_{eff} A_f} \tag{3.31}$$

It is important to note that the solid heat capacities used in the utilization and symmetry parameters in this case would be constant-field heat capacities, c_B and $c_{B,ref}$.

3.2.2 AMR Energy Balance

The general form solid energy balance relation, given by Equation (3.29) can be used to derive the AMR energy balance equation but the analysis is complicated by the presence of magnetic work transfer as the source term in this case. This term is a result of a change in the intensity of the magnetic field that is being applied to a magnetocaloric material and is not a simple source term. The following expressions for the solid internal energy, U_s, and magnetic work transfer, $\dot{W}_{mag}$, are necessary for the analysis:

$$\begin{aligned} dU_s &= M_s du_s = \left(\rho_s A_s dx\right) du_s \\ \dot{W}_{mag} &= M_s \dot{w}_{mag} = \left(\rho_s A_s dx\right) B \frac{\partial m}{\partial t} \end{aligned} \tag{3.32}$$

where, M_s is the mass of the solid, u_s is the specific (per unit mass) internal energy, ρ_s is the density of the solid, A_s is the area of magnetocaloric material for a given cross-section, $\dot{w}_{mag}$ is the mass specific rate of magnetic work, B is the applied magnetic field ($B = \mu_0 H$), and m is the magnetization per unit mass. Substituting these relations and those defined in Equation Set (3.22) into the solid energy balance equation, grouping the internal energy and magnetic work terms, and dividing through by dx,

$$\rho_s A_s \left(\frac{\partial u_s}{\partial t} - B \frac{\partial m}{\partial t} \right) = \frac{\partial}{\partial x} \left(k_s A_s \frac{\partial T_s}{\partial x} \right) + h P_w \left(T_f - T_s \right) \tag{3.33}$$

It is necessary to manipulate the left-hand side of this equation before relating this form of the solid energy balance equation to the general form equation developed in Section 3.1.2. Rearranging the Tds relation for magnetic materials suggests that it is necessary to obtain an expression for the entropy change, ds, in order to transform Equation (3.33) into a more manageable form:

$$\begin{aligned} du &= Tds + Bdm \\ \therefore \frac{du}{dt} - B\frac{dm}{dt} &= T\frac{ds}{dt} \end{aligned} \tag{3.34}$$

The entropy of a magnetic material is a function of both its temperature, T, and the magnetic field applied to it, B (i.e. $s = f(T, B)$). Therefore, it follows that:

$$ds = \left(\frac{\partial s}{\partial T} \right)_B dT + \left(\frac{\partial s}{\partial B} \right)_T dB \tag{3.35}$$

where, the subscripts B and T denote constant applied field and temperature processes, respectively. By definition, for a constant field process with no net work input,

$$\left. \frac{\partial s}{\partial T} \right|_B = \frac{c_B}{T} \tag{3.36}$$

where, c_B is the constant-field specific heat. Also, using Maxwell's relation,

$$\left(\frac{\partial s}{\partial B}\right)_T = \left(\frac{\partial m}{\partial T}\right)_B \tag{3.37}$$

Substituting Equations (3.36) and (3.37) into Equation (3.35) and arranging into the form required by the energy balance equation,

$$\left(\frac{\partial u_s}{\partial t} - B\frac{\partial m}{\partial t}\right) = T_s\frac{ds}{dt} = \left(c_B\frac{\partial T_s}{\partial t} + T_s\left(\frac{\partial m}{\partial T}\right)_B\frac{\partial B}{\partial t}\right) \tag{3.38}$$

Substituting this expression into the AMR energy balance equation, (3.33), applying Equations (3.6) and (3.7) to eliminate the wetted perimeter term, P_w, and impose non-dimensionalized units of time and space, and rearranging yields:

$$\frac{\partial T_s}{\partial t^*} = \frac{1}{c_B}\frac{\partial}{\partial x^*}\left(\frac{k_s\tau}{\rho_s L^2}\frac{\partial T_s}{\partial x^*}\right) + \frac{hA_w\tau}{M_s c_B}\left(T_f - T_s\right) - \frac{T_s}{c_B}\left(\frac{\partial m}{\partial T}\right)_B\frac{\partial B}{\partial t^*} \tag{3.39}$$

Except for the magnetic work term and the use of constant field specific heat, this expression is identical to Equation (3.24). Thus, only the magnetic work term needs to be manipulated further and the remainder of the equation can be obtained from the general form solid energy balance equation, developed in Section 3.1.2. The magnetic work term can be simplified if an isentropic magnetization, $ds = 0$, is assumed:

$$\begin{aligned}
&\left(c_B\frac{\partial T_s}{\partial t} + T_s\left(\frac{\partial m}{\partial T}\right)_B\frac{\partial B}{\partial t}\right) = 0 \\
&\therefore d(\Delta T_{ad}) = -\frac{T_s}{c_B}\left(\frac{\partial m}{\partial T}\right)_B dB \\
&\therefore \frac{d(\Delta T_{ad})}{dB} = -\frac{T_s}{c_B}\left(\frac{\partial m}{\partial T}\right)_B
\end{aligned} \tag{3.40}$$

where, ΔT_{ad} is the adiabatic temperature change due to the magnetocaloric effect. Hence, a modified version of the general form solid energy balance is obtained:

$$\frac{\partial T_s}{\partial t^*} = \psi \frac{\partial}{\partial x^*}\left(\frac{1}{\mathrm{Ks}}\frac{\partial T_s}{\partial x^*}\right) + NTU\,\phi(T_f - T_s) + \frac{d(\Delta T_{ad})}{dB}\frac{dB}{dt^*} \tag{3.41}$$

The conductivity term is dropped since the conductivity of the solid is incorporated into an effective conductivity term in the fluid equation, as described in Section 4.1.1. This yields the final form of the AMR solid energy balance equation:

$$\frac{\partial T_s}{\partial t^*} = NTU\,\phi(T_f - T_s) + \frac{d(\Delta T_{ad})}{dB}\frac{dB}{dt^*} \tag{3.42}$$

It should once again be noted that the solid heat capacity used in the utilization term of this expression is the constant-field heat capacity, c_B.

3.3 Cold Section

A similar analysis, based on the general equations developed in Section 3.1, is conducted in order to obtain the equivalent coupled one-dimensional fluid and solid energy balance equations describing the energy transfer within the cold section. This section was modeled as a fluid flowing through a tube with possible heat loads being applied to represent heat leaks into the system or the refrigeration of a load.

3.3.1 Fluid Energy Balance

The general fluid energy balance expression, given by Equation (3.19), can be used to derive the energy balance for the fluid flowing within the cold section if the source term is used to denote applied heat loading. This heat load input term represents the application of a distributed heat load across the cold section to mimic operation with a particular cooling power.

$$\kappa \frac{\partial T_f}{\partial t^*} = -\phi \frac{\partial T_f}{\partial x^*} + \psi \frac{\partial}{\partial x^*}\left(\frac{\phi_{ref}}{Pe_f} \frac{\partial T_f}{\partial x^*} \right) + NTU\,\phi(T_s - T_f) + \frac{\dot{Q}_{load}\tau}{M_s c_s} \tag{3.43}$$

where, $\dot{Q}_{load}$ is used to represent the heat load input. It is important to point out that an effective conductivity expression is not used in this case and the cold section solid heat capacity is independent of magnetic field intensity.

3.3.2 Solid Energy Balance

The energy balance expression for a section of tubing with fluid flowing through it can be derived from the general solid energy balance relation of Equation (3.29) if the source term is used to represent a radiative heat load into the system. This term represents radiative heat transfer between the surroundings and the outside wall of the tubing. Thus, the energy balance equation for the cold section solid becomes:

$$\frac{\partial T_s}{\partial t^*} = \psi \frac{\partial}{\partial x^*}\left(\frac{1}{\mathrm{Ks}} \frac{\partial T_s}{\partial x^*} \right) + \mathrm{NTU}\,\phi\left(T_f - T_s\right) + \frac{\dot{Q}_{rad}\tau}{M_s c_s} \tag{3.44}$$

Expansion of the radiative heat load source term is also considered:

$$\dot{Q}_{rad} = \sigma A_{w,o} R\left(T_\infty^4 - T_s^4\right) \tag{3.45}$$

where, $A_{w,o}$ is the outer area of the tubing subjected to a radiative load, σ is the Stefan-Boltzmann constant, R is the radiative resistance between the outside of the tube and the inner wall of the apparatus, and T_∞ is the temperature of the of the surroundings with which the radiative heat transfer occurs.

3.4 Boundary and Initial Conditions

Due to the cyclic nature of the flow in the AMRTA cylinder, as shown in Figure 2.2, it is necessary to impose periodic boundary conditions:

$$\dot{m} >= 0, \qquad \begin{aligned} @\, x = 0: &\quad T_f = T_H \\ @\, x = 3L: &\quad \frac{\partial T_f}{\partial x} = 0 \end{aligned} \tag{3.46}$$

$$\dot{m} < 0, \qquad \begin{aligned} @\, x = 0: &\quad \frac{\partial T_f}{\partial x} = 0 \\ @\, x = 3L: &\quad T_f = T_H \end{aligned} \tag{3.47}$$

where, T_H is the hot heat sink temperature, and a positive mass flow rate indicates fluid flow in the positive x direction and vice versa. These conditions are set such that the fluid temperature at the inlet boundary is equal to the hot heat sink temperature while the boundary condition at the model domain outlet specifies that there is no heat flux at this point. The boundaries between the AMR sections and the cold section and any boundaries between AMR sub-domains used to represent different materials are all assumed to be continuous. Further, the initial condition assumes that the temperature across the model domain is uniform and is set to the hot heat sink temperature.

Chapter 4 – Material Properties and Correlations

Consulting the governing energy balance equations derived in Chapter 3, a number of thermophysical and transport properties are needed to properly describe the flow of energy within the system. This chapter describes how these quantities are obtained for both the AMR sections and the cold section.

4.1 AMR Sections

4.1.1 Heat Transfer Fluid

Helium is used as the heat transfer fluid flowing within the AMR sections. It is necessary to obtain values for several of the fluid properties, as well as the convection coefficient between the fluid and the porous bed and the effective conductivity of the system, taking into account the effects of dispersion.

Fluid Properties

Helium density is calculated using the ideal gas equation. This is a reasonable assumption considering that helium is monatomic. In fact, a deviation of less than 0.5% is found between densities obtained from data tables and those calculated using the ideal gas law in the temperature and pressure ranges being considered (240-320 K and 3-15 atm). Other helium properties are obtained from the National Institute of Standards and Technology's (NIST) online database of thermophysical properties [20]. The properties are obtained over a large range of temperatures and for the maximum operating pressure of the AMRTA. Curve fits of this data allow for interpolation of the properties to be made at any given temperature. Simulations with other pressures assume that the helium properties other than density do not vary with pressure. This is also a very reasonable assumption considering that values of specific heat, conductivity, and viscosity are found to vary by less than 0.4% over the pressure range being considered.

Convection Coefficient

The convection coefficient is used in the calculation of the term describing energy transfer between the porous regenerator matrix and the heat transfer fluid as a

result of convection. The expression for the heat transfer coefficient within a porous bed is usually of the form [21]:

$$h = j_H G c_p \,\mathrm{Pr}^{-2/3} \tag{4.1}$$

where, h is the convection heat transfer coefficient, j_H is the Colburn j-factor, G is the mass velocity or the mass flow rate per unit fluid flow area, and c_p and Pr are the specific heat and Prandtl number of the fluid, respectively. Many correlations are available for the Colburn j-factor; Barron references a correlation for spherical regenerator particles from Kays and London [21]:

$$j_H = 0.23\,\mathrm{Re}^{-0.3} \tag{4.2}$$

The expressions for the mass velocity and the Reynolds number are as follows:

$$G = \frac{\dot{m}}{A_f} \tag{4.3}$$

$$\mathrm{Re} = \frac{G D_h}{\mu} \tag{4.4}$$

where, $\dot{m}$ is the mass flow rate, A_f is the fluid flow area, also commonly known as the free-flow area, D_h is the characteristic dimension for the analysis (the hydraulic diameter in this case), and μ is dynamic viscosity of the fluid. The hydraulic diameter can be calculated from the equivalent spherical diameter such that [21]:

$$D_h = \frac{2\alpha D_{eq}}{3(1-\alpha)} \tag{4.5}$$

where, α is the porosity of the regenerator, and D_{eq} is the equivalent spherical diameter. For a spherical particle regenerator, the average particle diameter can

simply be used. For flaked particle beds, however, the following expression applies [22]:

$$D_{eq} = \frac{6V_p}{A_p \phi_s} \tag{4.6}$$

where, V_p and A_p are the volume and surface area of an average particle, respectively, and ϕ_s is Gamson's shape factor, also known as the sphericity. For flaked particles, Gamson's shape factor is 0.86 [22]. Also, flaked particles can be modeled as prismatic structures such that:

$$\begin{aligned} V_p &= l_p w_p h_p \\ A_p &= 2l_p w_p + 2w_p h_p + 2l_p h_p \end{aligned} \tag{4.7}$$

where, l_p, w_p, and h_p are the length, width, and height of an average particle.

Effective Conductivity

The effective conductivity is a local volume-averaged property and is dependent on the conductivity of each phase and the porosity of the porous media [23]. Although this quantity is principally derived for the type of analysis where the fluid and solid phases are in thermal equilibrium, it can also be used when this assumption is not valid and two-medium treatment is required. For instance, the dispersion-particle-based model, an accurate and widely used model for transient problems, includes the effective thermal conductivity in the fluid phase equation and accounts for only radial conduction in the solid phase equation [23]. Thus, with one-dimensional analyses, conduction can be eliminated completely from the solid energy balance. The effective conductivity can be expressed as [14]:

$$k_{eff} = k_{static} + k_f D^d \tag{4.8}$$

where, k_{eff} is the effective conductivity, k_{static} is the static component of the effective conductivity, k_f is the conductivity of the fluid phase, and D^d is the dispersion coefficient. The static component of the effective conductivity is

essentially the effective conductivity of the packed bed when there is no flow. Although several correlations exist for this quantity, the one developed by Hadley is the most recent and uses the most detailed approach [23]:

$$k_{static} = k_f \left[\left(1-\alpha_o\right) \frac{\alpha f_o + \frac{k_s}{k_f}\left(1-\alpha f_o\right)}{1-\alpha\left(1-f_o\right)+\frac{k_s}{k_f}\alpha\left(1-f_o\right)} + \alpha_o \frac{2\left(\frac{k_s}{k_f}\right)^2\left(1-\alpha\right)+\left(1+2\alpha\right)\frac{k_s}{k_f}}{\left(2+\alpha\right)\frac{k_s}{k_f}+1-\alpha} \right] \tag{4.9}$$

where, k_s is the conductivity of the solid and α is the porosity of the packed bed. The constants α_o and f_o are defined as:

$$f_o = 0.8 + 0.1\alpha$$

$$\begin{aligned} \log \alpha_o &= -4.898\alpha & 0 \le \alpha \le 0.0827 \\ \log \alpha_o &= -0.405 - 3.154\left(\alpha - 0.0827\right) & 0.0827 \le \alpha \le 0.298 \\ \log \alpha_o &= -1.084 - 6.778\left(\alpha - 0.298\right) & 0.298 \le \alpha \le 0.580 \end{aligned} \tag{4.10}$$

The second element of Equation (4.8) is the dynamic component of the effective conductivity. This accounts for fluid mixing, or dispersion, as it travels through the porous bed. It is convenient to model this as an additional conduction loss. Although the magnitude of the dispersion coefficient varies quite significantly, its form is always quite similar. A recent correlation that yields average results compared to others is chosen for this analysis [14]:

$$D^d = 0.75\alpha\,\mathrm{Pe} \tag{4.11}$$

where, Pe is the Peclet number which is defined as:

$$\mathrm{Pe} = \mathrm{Re}\,\mathrm{Pr} \tag{4.12}$$

where, Re and Pr are the dimensionless Reynolds and Prandtl numbers. It should be noted that the same definition for the Reynolds numbers is used in this case as is given in Equation (4.4).

4.1.2 Magnetocaloric Material

It is also necessary to obtain the values of several key parameters for the magnetocaloric material in the AMR sections. This includes material properties such as heat capacity, conductivity, and temperature changes due to the magnetocaloric effect. The convection heat transfer coefficient, whose expression is shown in the heat transfer fluid section, is also used.

Magnetocaloric Material Properties

Material properties such as density, conductivity, and heat capacity are obtained from several sources [10, 24, 25] for the materials in question. Density and conductivity are assumed to be constant while heat capacity data at several field intensities is used to determine the heat capacity for a given temperature and field intensity. Interpolation techniques are used to accomplish this.

Magnetocaloric Effect Function

With the magnetic field intensity varying sinusoidally and simultaneously with the mass flow rate, a simple step function application and removal of temperature changes due to the magnetocaloric effect cannot be used. Instead, it is necessary to construct an MCE function that can mimic the gradual temperature changes due to the magnetic field changing over time. This function is based on the current regenerator temperature, T_r, the magnetic field intensity, B, and the rate of change of the magnetic field intensity, dB/dt. Having a function that is based on the current temperature is a complication since all the magnetocaloric effect data that is available is based on the initial, zero-field temperature.

The first step is to develop a function that can estimate the temperature changes incurred due to the step-function application of a given magnetic field (e.g. 0-1 T). For Gd, for example, this is done by using the magnetocaloric effect data for this material and a 0-2 T field change [10] as a baseline curve that can be scaled using the maximum MCE at a specified field intensity. Since MCE data is only available for a few applied fields, it is necessary to obtain a curve fit of the maximum MCE as a function of field intensity, $\left(\Delta T_{ad}\right)_{\max} = f(B)$. This allows for

proper scaling of the baseline, 0-2 T curve so that it is possible to find the MCE at a given temperature and for a field change of 0-B T.

With this function available, it is possible to create another function that can be used to apply an incremental temperature change due to the magnetic field changing over time. It is convenient to expand the expression for temperature change (due to the magnetocaloric effect) per unit time, as can be seen in Equation (4.13). With the rate of change of the magnetic field, dB/dt, set in the simulation, it is necessary to construct a function to calculate the temperature change per unit field change, $d\left(\Delta T_{ad}\right)/dB$.

$$\frac{d\left(\Delta T_{ad}\right)}{dt} = \frac{d\left(\Delta T_{ad}\right)}{dB}\frac{dB}{dt} \tag{4.13}$$

The temperature change per unit field change function is created by using the original MCE function to determine the temperature change at several fields for a specified temperature. A fourth-order polynomial fit is then applied to this data to obtain an expression for the MCE as a function of field for a particular initial temperature. This procedure is illustrated in Figure 4.1. Next, the polynomial expression can easily be integrated and evaluated at the current field intensity to yield the required value.

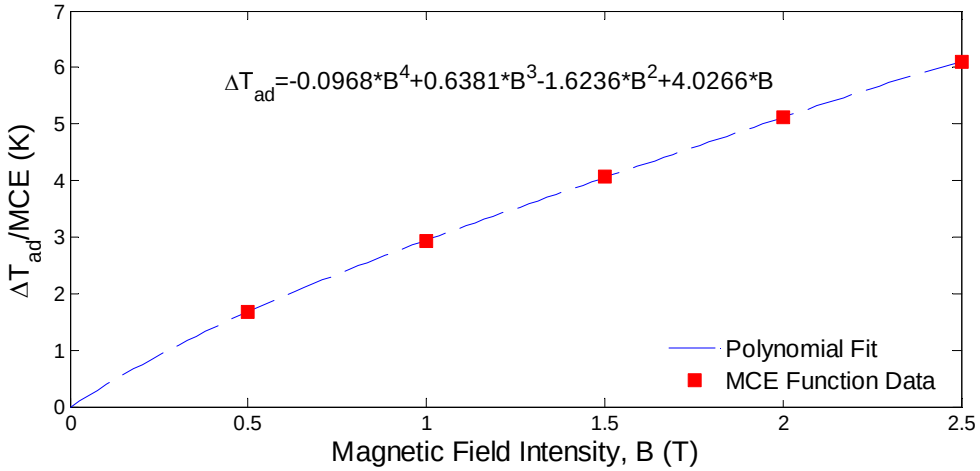

Figure 4.1 – A graphical depiction of the curve-fit procedure used by the temperature per unit field change function.

However, another complication arises with the $d(\Delta T_{ad})/dB$ function since it is based on the initial, zero-field temperature of the magnetocaloric material rather than its current temperature. This is because all available MCE data is based on the initial temperature. In order for the function to be used, it is necessary to create a routine that can determine the equivalent zero-field initial temperature based on the current temperature and magnetic field intensity. This is accomplished by generating a look-up table. The temperature change per unit field change function is used with a vector of initial temperatures and the magnetization procedure is simulated in order to obtain an array of data. An excerpt of this type of array for the magnetization process is shown in Figure 4.2. If, for instance, the magnetic field intensity is 0.04 T and the current temperature is 299.15 K, this array of data can be used to determine that the corresponding zero-field temperature is 299.0 K.

Magnetic Field Intensity (T)	**Initial (Zero Field) Temperature (K)**					
0.0000	300.00	***299.00***	298.00	297.00	296.00	295.00
	Magnetized Temperature (K)					
0.0067	300.02	299.02	298.03	297.03	296.03	295.03
0.0133	300.05	299.05	298.05	297.05	296.05	295.05
0.0200	300.07	299.07	298.08	297.08	296.08	295.08
0.0267	300.10	299.10	298.10	297.10	296.10	295.10
0.0333	300.12	299.12	298.13	297.13	296.13	295.13
0.0400	300.14	***299.15***	298.15	297.15	296.16	295.16
0.0467	300.17	299.17	298.18	297.18	296.18	295.18
0.0533	300.19	299.19	298.20	297.21	296.21	295.21
0.0600	300.21	299.22	298.23	297.23	296.23	295.23

Figure 4.2 – Excerpt from a sample magnetization simulation data array.

This procedure is used to calculate the required temperature difference per unit time as a result of the MCE during both the magnetization and demagnetization procedures. The sign of the rate of change of the magnetic field is used to account for direction of temperature change.

4.2 Cold Section

The properties described in this section are necessary to properly represent the energy transfer within the cold section. This is essentially modeled as the flow of

fluid through a hollow tube with a radiative load being applied to the outside of the tube and another heat load being applied to the fluid stream to simulate operation with a particular cooling power.

4.2.1 Heat Transfer Fluid

Fluid Properties

The fluid characterized in this section of the model domain is also helium. Fluid properties are obtained in the same manner as those for the fluid within the AMR sections, as described in Section 4.1.1.

Convection Coefficient Correlation

The convection coefficient in the cold section is used to characterize the flow of energy from the tubing to the heat transfer fluid as a result of fluid flow within the tube. Calculations with typical flow parameters and component dimensions, as specified in Tables 5.1 and 5.2, show that the Reynolds number of the flow is approximately 2000. For pipe flows, this Reynolds number is representative of a laminar flow. For a circular tube with uniform surface heat flux and laminar, fully-developed flow, the convection coefficient is of the form [26]:

$$h = 4.36\frac{k}{D} \tag{4.14}$$

where, k is the conductivity of the fluid and D is the diameter of the circular tube.

4.2.2 Cold Section Tube

The solid portion of the cold section is modeled as a G10-CR tube. Although pieces of phenolic tubing are actually present in portions of this passage in the AMRTA, they are neglected since they would essentially just add more thermal mass to the energy balance equation and postpone the convergence of simulations.

Solid Properties

High-order logarithmic polynomial fits for the thermal conductivity and heat capacity of G10-CR are obtained from the National Institute of Standards and

Technology (NIST) website [27]. These equations are reported to have errors up to 5% for the temperature range 10-300 K. The density of G10-CR is taken to be 1800 kg/m^3 [28].

Radiative Resistance Expression

The radiative resistance expression is used to help describe the flow of energy through radiation between the outside of the G10-CR cold section tube and the inner wall of the apparatus. This can be modeled as radiation transfer between two concentric cylinders, where the rate of heat transfer is [26]:

$$\dot{Q}_{rad} = \frac{\sigma A_1 \left(T_2^4 - T_1^4 \right)}{\frac{1}{\varepsilon_1} + \frac{1-\varepsilon_2}{\varepsilon_2}\left(\frac{r_1}{r_2} \right)} \tag{4.15}$$

where, $\dot{Q}_{rad}$ is the rate of radiative heat transfer from the outer cylinder to the inner cylinder, the subscripts 1 and 2 denote the inner and outer cylinders, respectively, σ is the Stefan-Boltzmann constant, A is the cylindrical surface area, T represents the cylinder temperatures, ε the emissivity of each of the cylinders, and r the radius of each of the cylinders. This implies that the radiative resistance, R, to be used with Equation (3.45) is:

$$R = \frac{1}{\frac{1}{\varepsilon_1} + \frac{1-\varepsilon_2}{\varepsilon_2}\left(\frac{r_1}{r_2} \right)} \tag{4.16}$$

4.3 System Properties

4.3.1 Mass Flow Rate Determination

Establishing an expression for the mass flow rate of heat transfer fluid within the system is a vital portion of the analysis. Two identical magnetically-coupled displacers are used to drive helium within the AMRTA. A representation of the piston-cylinder type assembly used to drive these displacers is shown in Figure 4.3. The crank, A-B, rotates about A and is attached to the connecting rod, B-C,

which is used to drive the displacer pistons, C, back and forth along the x-axis. The mass flow rate of fluid driven by the pistons is given by:

$$\dot{m} = 2\rho v A_d \tag{4.17}$$

where, $\dot{m}$ is the mass flow rate, ρ is the density of the fluid, and v and A_d are the velocity and surface area of each of the displacer pistons. The density of the fluid is known since the displacers operate at ambient temperatures. The surface area of each of the displacer pistons is also known. Therefore, it is only necessary to obtain an expression for the velocity of the piston displacers in order to determine the mass flow rate of heat transfer fluid within the system.

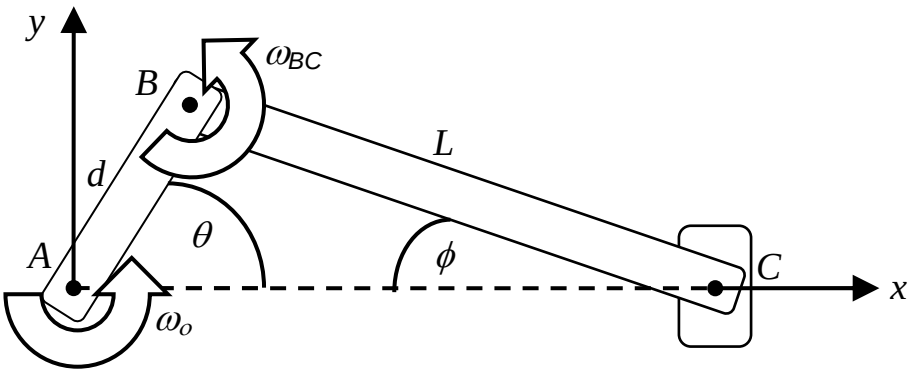

Figure 4.3 – Crank and connecting rod assembly used to drive the displacer.

Referring once again to Figure 4.3, a vector analysis can be used to obtain an expression for the velocity of the displacer pistons, C, along the x-direction. First, an expression for the velocity of point B must be found:

$$\vec{v}_B = \omega_o \vec{k} \times \vec{l}_{B/A} \tag{4.18}$$

where, $\vec{v}_B$ is the velocity vector at point B, ω_o is the rotational velocity about point A, and $\vec{l}_{B/A}$ is the distance vector relating point B to point A. It should also be noted that $\vec{i}$, $\vec{j}$, and $\vec{k}$ are used to represent unit vectors in the x, y, and z directions, respectively. The vector $\vec{l}_{B/A}$ can be expanded such that,

$$\vec{l}_{B/A} = d\cos\theta\vec{i} + d\sin\theta\vec{j} \tag{4.19}$$

Substituting this expression into Equation (4.18) and completing the cross product yields:

$$\vec{v}_B = \omega_o d\cos\theta\,\vec{j} - \omega_o d\sin\theta\,\vec{i} \tag{4.20}$$

The expression for the velocity at point C can now be derived:

$$\vec{v}_C = \vec{v}_B + \omega_{BC}\vec{k}\times\vec{l}_{C/B} \tag{4.21}$$

where, $\vec{v}_C$ is the velocity at point C, ω_{BC} is the rotational velocity of member BC about point B, and $\vec{l}_{C/B}$ is the distance vector between points B and C. This vector can be expanded such that:

$$\vec{l}_{C/B} = L\cos\phi\,\vec{i} - L\sin\phi\,\vec{j} \tag{4.22}$$

Substituting this and Equation (4.20) into Equation (4.21), completing the cross-product once again, and grouping terms,

$$\vec{v}_C = \left(-\omega_o d\sin\theta + \omega_{BC}L\sin\phi\right)\vec{i} + \left(\omega_o d\cos\theta + \omega_{BC}L\cos\phi\right)\vec{j} \tag{4.23}$$

However, there must be a vanishing $\vec{j}$ component since the piston movement is only along the x-axis. Setting the $\vec{j}$ portion to zero and solving for ω_{BC} yields:

$$\omega_{BC} = -\omega_o\frac{d\cos\theta}{L\cos\phi} \tag{4.24}$$

Substituting this into Equation (4.23), recognizing that the $\vec{j}$ component has been eliminated, and simplifying,

$$\vec{v}_C = -\omega_o d\left(\sin\theta + \cos\theta\tan\phi\right)\vec{i} \tag{4.25}$$

This relation can be simplified further when $L \gg d$, as is the case with the AMRTA. Referring to Table 5-2, $L/d \approx 5.4$, and so, $\tan\phi \approx 0$. Also recognizing

that $\theta = \omega_o t$ yields the final form of the equation for the velocity of the displacer pistons:

$$v_C = -\omega_o d \sin\left(\omega_o t\right) \tag{4.26}$$

4.3.2 Magnetic Field Intensity

A sinusoidal variation of the magnetic field intensity, with each of the AMRs being 180^o out of phase with the other, is used in the simulations. This type of field intensity variation is shown in Figure 2.2. The minimum field is not set to zero, however, since a plot of the relative field strength along the center of the magnets shows that the field intensity is still positive when each of the regenerators is at its maximum distance away from the magnet [11]. Instead, a value of 5% of the maximum is used for the magnitude of the minimum magnetic field intensity.

Chapter 5 – Model Implementation

This chapter outlines the integration of the governing equations into a finite element modeling package in order to simulate the AMR test apparatus. The parameters that are used in the simulations and the process used to validate the results are also outlined. Further, a short description of the experimental procedure is given.

5.1 Finite Element Modeling Package Integration

The finite element modeling (FEM) package Comsol Multiphysics^{TM}, previously known as FEMLAB^{TM}, is used to simulate the AMRTA. The transient partial differential equation (PDE), general form modeling option is used with two dependent variables in order to represent the solid and fluid temperatures throughout the model domain. The energy balance equations for each of the phases, derived in Chapter 3, are then input. The FEM package is able to communicate with MATLAB^{TM}, and so, functions to calculate the values of parameters are written in this program and employed within the model during the simulations. It should also be noted that a mesh consisting of 121 nodes is used and that the maximum time step is limited to 0.01 s. The values of these parameters are based on basic sensitivity analyses and attempts to minimize the processing time as much as possible. It is found that the size of the time steps has a much larger impact on the processing time than the mesh size.

Based on the analysis conducted in Section 4.3.1, a sinusoidal variation of the fluid mass flow rate allows for the alternating blow directions to be simulated. This, coupled with the sinusoidal magnetic field intensity variation, as described in Figure 2.2 and Section 4.3.2, and the mass flow rate dependent boundary conditions, described in Section 3.4, allow for a model of the AMRTA refrigeration cycle to be produced.

This alternating blow direction and magnetization-demagnetization cycle is repeated many times in the hope that the temperature profiles of the fluid and regenerator attain a steady state condition, as seen with the experimental

apparatus. However, it is found that some modifications to the governing equations are required in order for the simulations to converge properly. These changes include the following:

1. The transient term in the cold section solid equation, as shown in Equation (3.44), is neglected. This term represents the rate of change of the internal energy of the solid in the cold section. It is neglected because the simulations are taking much too long to converge. By omitting this term, only the thermal mass of the gas is accounted for in the cooling process and the rate of simulation convergence is found to be greatly improved. Tests confirm that this change has a negligible effect on the steady state condition achieved.
2. The radiative load in the cold section solid energy equation is moved to the cold section fluid energy equation. This change is required due to the omission of the transient term in the cold section solid energy equation. Leaving the radiative term in the solid equation without the transient term causes the cold section solid to heat up too quickly and results in sharp gradients at the boundaries between the cold section and the AMR sections. Even a small radiative load then results in a large drop in the temperature span across the regenerators. Although placing the radiative load in the cold section fluid equation assumes that the load travels directly to the fluid, reasonable results, consistent with heat load experiments, are obtained if this approach is used.

The modified form of the cold section fluid and solid equations are given by the following:

$$\kappa \frac{\partial T_f}{\partial t^*} = -\phi \frac{\partial T_f}{\partial x^*} + \psi \frac{\partial}{\partial x^*}\left(\frac{\phi_{ref}}{\mathrm{Pe}_f} \frac{\partial T_f}{\partial x^*} \right) + NTU\,\phi (T_s - T_f) + \frac{\left(\dot{Q}_{load} + \dot{Q}_{rad} \right)\tau}{M_s c_s} \qquad (5.1)$$

$$\psi \frac{\partial}{\partial x^*}\left(\frac{1}{\mathrm{Ks}} \frac{\partial T_s}{\partial x^*} \right) + \mathrm{NTU}\,\phi \left(T_f - T_s \right) = 0 \qquad (5.2)$$

These expressions are modified forms of Equations (3.43) and (3.44). The definition of the notation can be found in the chapter outlining the derivation of the governing equations. The AMR section equations are not shown here since they are not modified. Thus, the modified cold section energy balance equations, (5.1) and (5.2), are used in conjunction with the AMR section energy balance equations, (3.30) and (3.42), to describe the flow of energy within the FEM package.

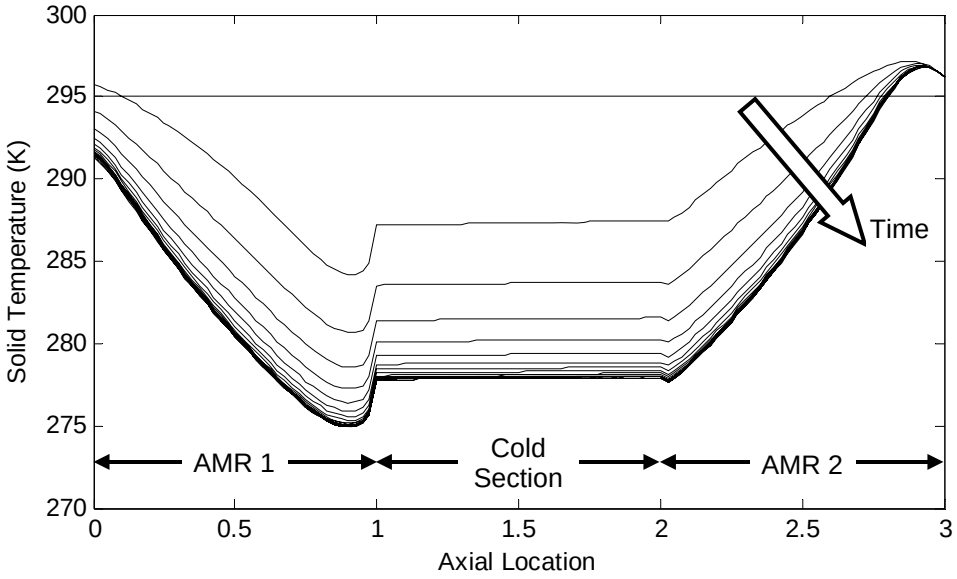

Figure 5.1 – Transient temperature profile of the simulated solid temperature throughout the model domain.

With these adjustments, the simulations begin to converge within a reasonable number of cycles. Since the alternating mass flow rate direction within the model produces some instability in the fluid temperature at low mass flow rates, this temperature cannot be used for convergence testing. Instead, convergence of the temperature span, defined as the difference between the hot heat sink temperature and the average temperature of the solid at the middle of the cold section, is tested over several cycles. Steady state is said to be achieved when the transient profile of the solid within the cold section has flattened off and the relative temperature span changes between subsequent cycles are less than 10^{-2} K. Figure 5.1 gives a good graphical representation of simulation convergence by depicting the transient temperature profile of the solid throughout the model

domain at five cycle intervals for a Gd simulation. The initial profile is uniform at 295 K and, as time passes, the curves begin to converge. The final temperature of the cold section in this case is approximately 278 K.

5.2 Simulation Parameters

The values of key operating parameters are summarized in Table 5-1. This table compares the model input parameters to the operating condition ranges currently possible with the apparatus.

Table 5-1 – A summary of several key operating parameters used in the simulations.

Operating Variable	Model Input	Apparatus
Magnetic Field Intensity, Max (T)	2.0	0-5.0
Magnetic Field Intensity, Min (T)	0.1	$0.05*B_{max}$
Frequency (Hz)	0.65-0.8	0.2-1.2
Hot Heat Sink Temperature (K)	270-310	263-313
Average Pressure (atm)	3.0-15.0	0-10.0
Cooling Load (Heaters) (W)	0-10.0	0-40.0
Ambient Temperature (K)	300	~300

Table 5-2 – A summary of properties and dimensions required by the simulations.

Regenerator (per puck)	
Mass (kg)	0.045
Length (cm[in])	2.54 [1.00]
Diameter (cm[in])	2.54 [1.00]
Porosity	0.56
Particle Size (μm)	335
Cold Section, Tubing	
Material	G10-CR
Length (cm[in])	15.24 [6.00]
Inner Diameter (cm[in])	3.18 [1.25]
Outer Diameter (cm[in])	3.81 [1.50]
Emissivity	0.85
Cold Section, Apparatus Inner Wall	
Material	Stainless Steel
Diameter (cm[in])	19.05 [7.50]
Emissivity	0.22
Gas Displacer	
Crank Length (cm[in])	10.16 [4.00]
Connecting Rod Length (cm[in])	54.61 [21.50]
Displacer Diameter (cm)	4.00

The values of physical parameters used in the simulations are summarized in Table 5-2. These values are obtained by direct measurement of the AMR test

apparatus. Others are obtained from references and require that certain assumptions be made. For instance, the emissivity value for the cold section tubing material is not readily available, and so, it is assumed that the value of this parameter is similar to that of Teflon since it is also a long-chained polymer.

5.3 Validation Procedure

Before the model can be used to predict the behaviour of the AMR test apparatus, it is necessary to validate simulation results by comparing them with experimental results. First, baseline model results with no additional losses are generated. Conduction and dispersion are the only loss mechanisms accounted for in these simulations and their magnitude is based on the correlations described in the previous chapter. As expected, this step is found to yield temperature spans that are significantly larger than those obtained experimentally. The accuracy of the simulation results is improved if radiative heat transfer into the cold section is accounted for. The amount of radiation can be adjusted by varying the length of the solid cylinder subjected to the radiative load. It is reasonable to vary this parameter since it is difficult to obtain an accurate measurement of the length of this section from the test apparatus. This is mainly due to the fact that the radiative path to the cylinder is partially obstructed by some fluid flow piping. The environmental reference temperature that is used can also be adjusted.

In order to account for parameter errors and experimental losses and produce results that are more consistent with experiments, the adjustment of several other parameters is also considered. For instance, for several reasons, there is a low level of confidence in some of the properties and correlations obtained to calculate the effective conductivity of the AMR section. This is largely a result of the regenerators being fabricated in house with flaked particles. Since correlations are generally based on relatively low porosity regenerator beds composed of spherical particles, it is necessary to employ corrections for the particles used. Adjustments in conductivity are also a practical location to account for heat leaks that are present experimentally but not accounted for in

the simulations since this accounts for the fact that the heat leaks into the system increase both with larger temperature spans and increasing regenerator lengths. Adjustments to the effective conductivity can be made either by adjusting the static or dynamic components of this parameter, k_{static} or D^d, respectively.

Adjustments to the value of the peak MCE of the materials being used is also considered. This accounts for impurities that may be present in the materials being tested experimentally in the AMRTA. These impurities tend to decrease the magnitude of the MCE. Further, there is also the possibility that the material tested in the experimental apparatus is of a higher purity than that used to obtain the reference data. In this case, the magnitude of the peak MCE can be adjusted to a higher level in the simulations. The Curie temperature of the material being used may also be modified. The reported values of this quantity vary by as much as 5 K, so adjusting this parameter is not unreasonable. This also accounts for the possibility of a slightly different composition than expected for a regenerator material composed of two or more elements (e.g. $Gd_{0.85}Er_{0.15}$).

These parameters are found to have very different effects on the simulated AMR performance. Increasing the degree of radiation that the cold section is subjected to tends to decrease the temperature span most for colder hot heat sink temperatures. However, AMR performance at hot sink temperatures above the Curie temperature is found to be less sensitive to heat loading with the addition of radiative loads in the cold section [29]. The performance is also found to deteriorate more quickly with decreasing pressure if radiation is accounted for. This aids in producing results that are more consistent with experiments.

Increasing the value of the static conductivity is found to have the largest impact on the higher end of the temperature variation curves. This behaviour is intuitive since the largest temperature spans are found here and the magnitude of heat leak due to conductivity scales with temperature span. AMR performance can also be more sensitive to losses in this region. The relative magnitude of the dynamic component of the effective conductivity is found to be much smaller and since it is flow rate dependent, its average impact is further diminished.

Consequently, scaling of this parameter is found to have a smaller and more uniform effect on the simulated AMR performance. As is expected, adjustment of the peak MCE value and the Curie temperature results in scaling and translation of the temperature variation curves.

Some care is taken to adjust these parameters so that results consistent with experiments can be obtained, but the parameter values are not properly optimized since this is a time-consuming exercise. It is also important to keep in mind that a fairly large measurement error of at least ±0.5 K is associated with the experimental results [29]. Instead, the aim is to obtain trends that are consistent with tests conducted with the AMR test apparatus. It is found that fairly good fits to experimental data can be obtained if radiative loading is accounted for and the static component of the effective conductivity is adjusted. As will be discussed in the validation results section, however, it is also necessary to adjust both the peak MCE value and the Curie temperature in the case of the $Gd_{0.85}Er_{0.15}$ AMR simulations.

5.4 Experimental Procedure

The AMR test apparatus has been used to examine the performance of regenerators composed of up to three different materials [29]. Multi-puck regenerators made up of a single material have also been tested so that their performance can be used as a baseline for comparison. As depicted in Figure 5.2, AMRs are created by stacking individual pucks, each roughly 2.54 cm (1.0 in) in both internal diameter and height.

To account for the varying regenerator lengths, spacers must be used to ensure that each of the AMRs is properly centred within the cylinder and is thus subjected to essentially the same magnetic field. As shown in Figure 5.3, Platinum Resistance Thermometers (PRTs) are placed at several locations so that the temperature at each of these areas can be monitored. This allows for both the total temperature span and the temperature span across each of the pucks to be determined. In the figure, T_H, T_I, and T_C represent the hot,

intermediate, and cold temperatures, respectively. There is usually some discrepancy between the spans measured on the top and bottom regenerators but it is generally less than 0.5 K in magnitude.

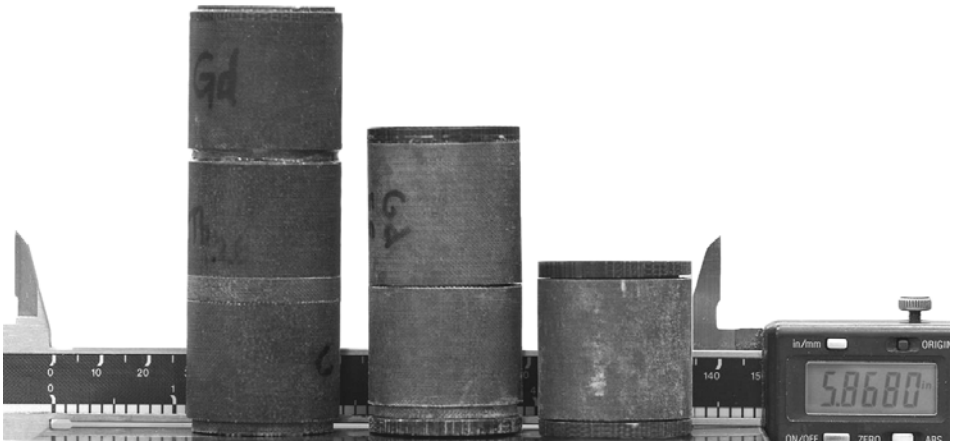

Figure 5.2 – Individual pucks are stacked to create multi-layer AMRs.

Experiments begin with fairly uniform temperature profiles throughout the system. For experiments near room temperature, the hot heat sink temperature is controlled through the use of a recirculating chiller. Employing this device, the temperature of a water-glycol mixture is set to a value between 270 K and 310 K. This fluid flows through heat exchangers that are adjacent to the hot ends of the AMRs and is essentially responsible for the heat rejection step of the refrigeration cycle.

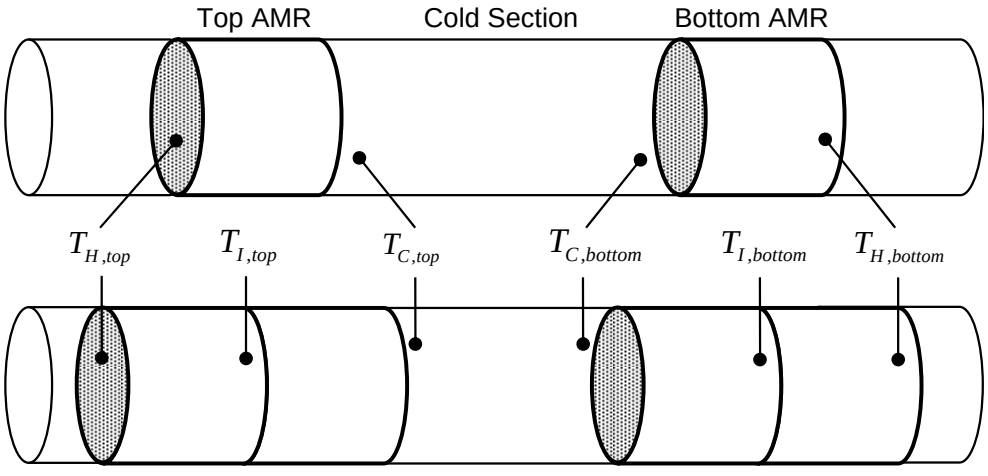

Figure 5.3 – Placement of temperature sensors for single and double puck AMR tests.

Based on the chosen hot heat sink temperature and other operating parameters, a temperature span begins to develop across each of the regenerators. Tests are allowed to progress until a steady state condition is achieved, as shown in the two puck experiment depicted by Figure 5.4. Single puck tests have been found to converge in about 40 min while tests with multiple puck regenerators take significantly longer to converge. In fact, the convergence time increases by approximately 70% for each puck that is added. This is only a guideline, however, since convergence time can be greatly reduced if the system is pre-cooled or if a portion of the beginning of a test is conducted with a lower hot heat sink temperature. One of the biggest challenges of conducting these tests is ensuring that the heat leaks into the system are consistent for each of the experiments. Thus, the rails that the cylinder moves along must be sufficiently pre-cooled before an experiment is begun. More detailed accounts of the experimental setup and procedure are available from other sources [9, 11, 29].

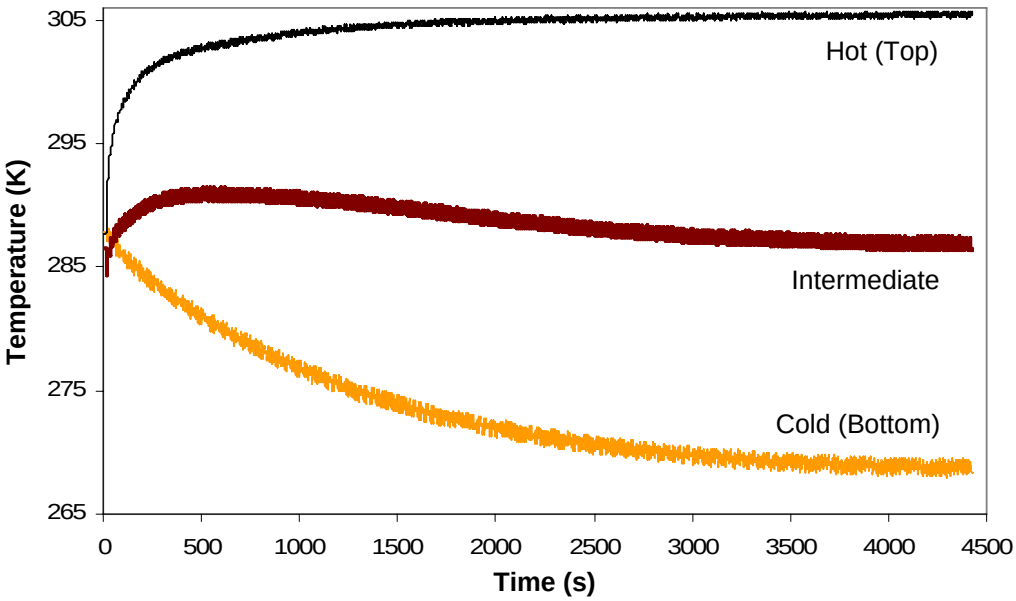

Figure 5.4 – The temperatures at different locations throughout a Gd-$Gd_{0.74}Tb_{0.26}$ AMR test operating at 9.5 atm and 0.65 Hz [29].

Chapter 6 – Model Validation Results

In an attempt to validate the model output, this chapter presents simulation results and compares them to the experimental results acquired from the AMRTA. This is done for both single and double puck regenerators and for varying hot heat sink temperature, system pressure, and applied heat load. Results with different simulated losses are presented. The baseline simulations, which are described as not having any additional losses, assume no radiative heat transfer to the cold section and no adjustment of the effective conductivity term used in the AMR sections. The abbreviation Rad, present in several of the following plots, represents the addition of a radiative heat load over a 15.24 cm (6.0 in) length in the cold section. The results of this analysis are discussed in more detail in Chapter 8.

6.1 Single Puck Simulations

Model results are obtained for Gd, $Gd_{0.74}Tb_{0.26}$, and $Gd_{0.85}Er_{0.15}$ single puck regenerators and compared to experimental results for the same materials. The most in-depth analysis, accounting for varying hot heat sink temperature, system pressure, and applied heat load, is performed with Gd. Only temperature variation results are obtained for the other materials. This is done based on the experimental data that is available for comparison. To be consistent with the experiments, all simulations except for heat load tests are conducted at an operating frequency of 0.65 Hz.

6.1.1 No-Load Temperature Variation

The first set of simulations examines the effect of hot heat sink temperature variation on the performance of the single puck regenerators. Hot heat sink temperature is an important operating parameter because it affects where an AMR operates with respect to the Curie temperature of the material that it is composed of (or the Curie temperatures in the case of multi-material AMRs). For tests near room temperature, setting the hot heat sink temperature in the simulations is analogous to adjusting the temperature of the recirculating chiller

discussed in Section 5.4. The metric used for the performance characterization of the AMRs is the magnitude of the temperature span developed across them. The results for the temperature variation behaviour of single puck Gd, $Gd_{0.74}Tb_{0.26}$, and $Gd_{0.85}Er_{0.15}$ AMRs are shown in Figures 6.1 to 6.3. As discussed in the validation procedure outlined in Section 5.3, to obtain simulation results that compare well with experimental data, model parameters are adjusted to account for various losses and heat leaks present in the experimental setup but not accounted for in the model.

Figure 6.1 depicts the fitting procedure that is used for Gd. The experimental data, represented by the solid points, shows that the peak temperature span is achieved at a hot sink temperature significantly above the Gd Curie temperature of approximately 295 K. Baseline model results are found to be significantly larger than the experimental results, with the largest deviation at higher temperatures. When radiation is considered, a drop is seen in the overall performance but the effect is most pronounced at lower temperatures. A good fit to experimental data is obtained with the Gd simulations if radiation is accounted for and the value of the conductivity is increased.

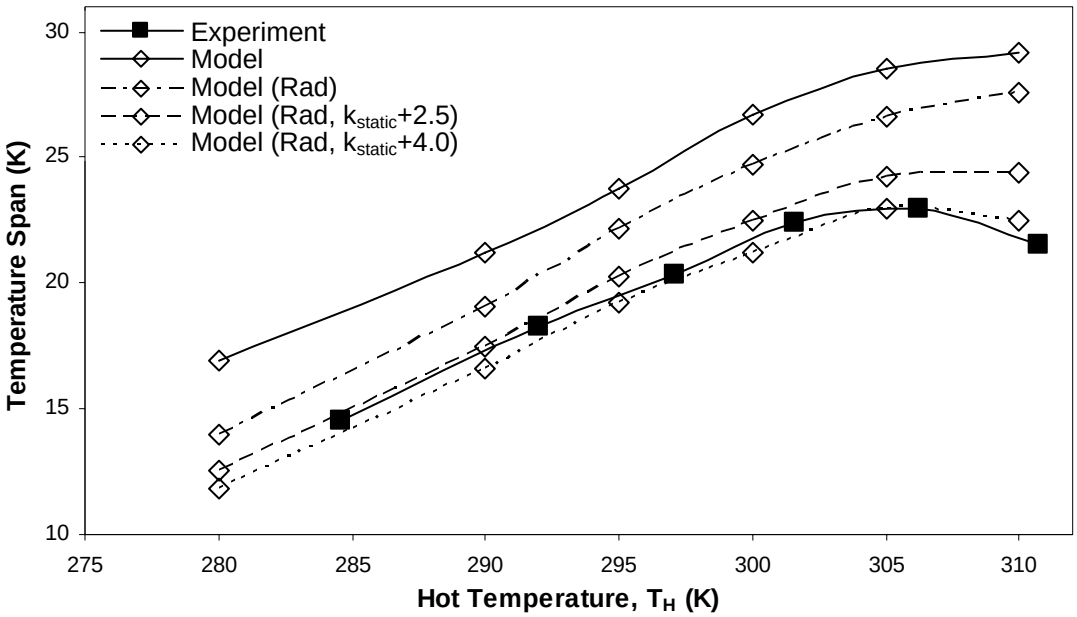

Figure 6.1 – Model results compared to experimental results for the temperature variation behaviour of Gd at 9.5 atm and 0.65 Hz.

Obtaining fitted model results with $Gd_{0.74}Tb_{0.26}$, and $Gd_{0.85}Er_{0.15}$ is a more challenging task. Figure 6.2 illustrates the fitting procedure for $Gd_{0.74}Tb_{0.26}$. In this case, the modifications used to acquire the most consistent results with the Gd simulations are used as the baseline. However, model results employing these parameters are found to be between 2.5 and 6.0 K higher than the experimental results obtained for this material. Simulation results that fit well with the experimental data are obtained if the static conductivity is increased further.

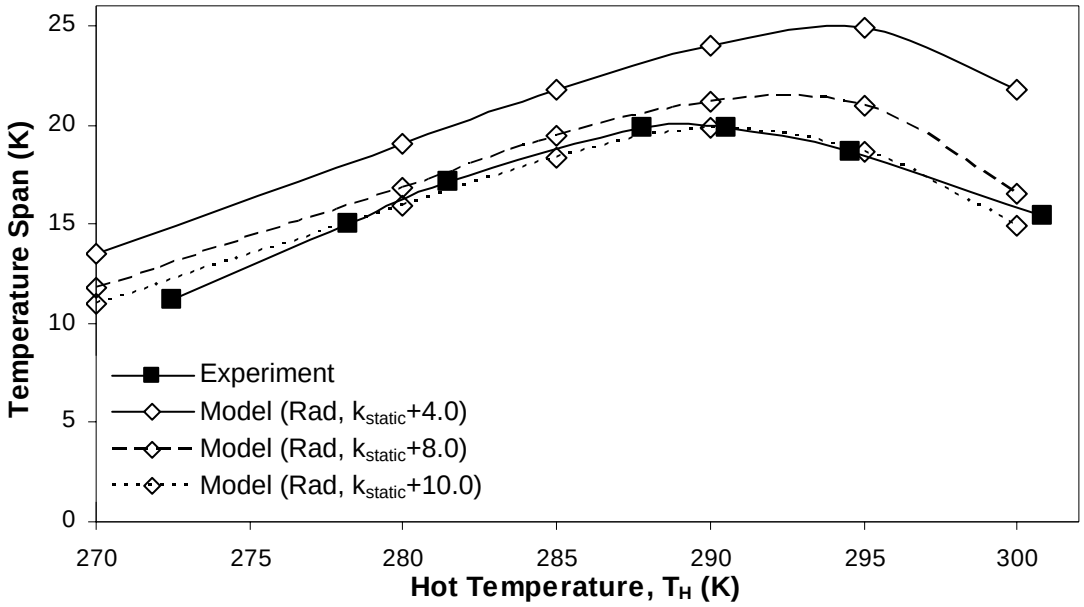

Figure 6.2 – The simulated temperature variation results for a $Gd_{0.74}Tb_{0.26}$ AMR compared to the experimental results, both at 9.5 atm and 0.65 Hz.

The process used to obtain model results that are in agreement with experimental data for the $Gd_{0.85}Er_{0.15}$ is depicted in Figure 6.3. For this material it is not possible to obtain a good fit to experimental results by only accounting for radiation and adjusting the value of the static conductivity, as is done with the other AMR simulations. Simulation results begin to better resemble experimental data if both the Curie temperature and the magnitude of the peak MCE are adjusted. It is also necessary to decrease the value of the static conductivity relative to the Gd simulations.

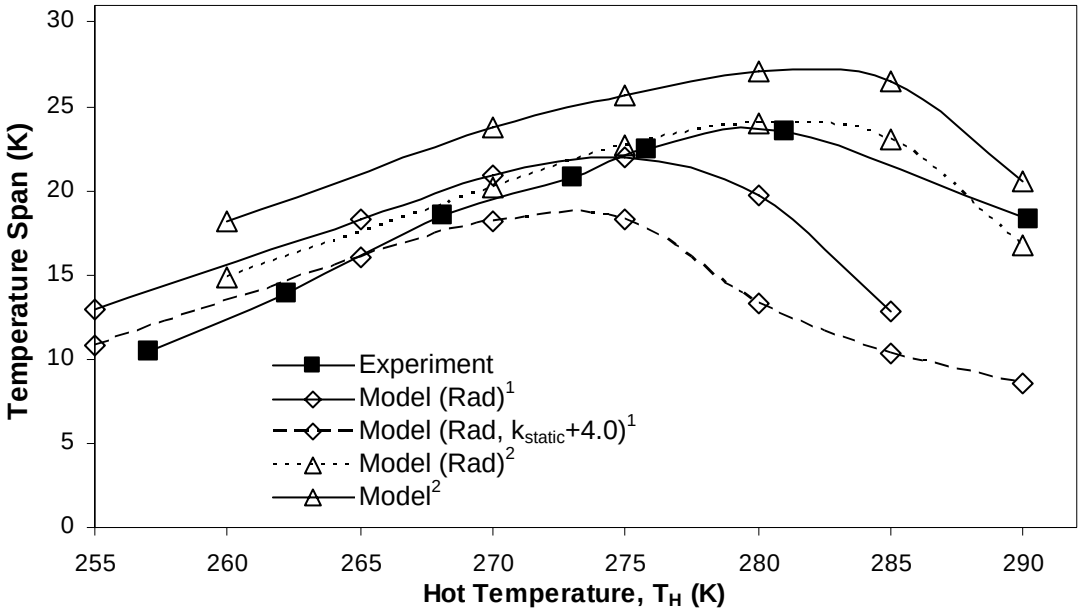

Figure 6.3 – Simulation validation results ([1] T_{curie}=261 K, MCE_{max}=4.5 K; [2] T_{curie}=265 K, MCE_{max}=5.0 K) for $Gd_{0.85}Er_{0.15}$ at 9.5 atm and 0.65 Hz.

Table 6-1 summarizes the parameters that are used to obtain simulation results that are most consistent with the experimental findings for single puck AMRs with varying hot heat sink temperature. The length of the radiative section and the dispersion scaling factor are not present in this summary table since these values are not adjusted in this analysis. Compared to Gd, it is found that a higher conduction loss is required in order to obtain fitted results for $Gd_{0.76}Tb_{0.24}$, while a shift in both the Curie temperature and peak MCE value, and a reduction in conduction loss are required for $Gd_{0.85}Er_{0.15}$. The significance of these modifications is examined in the discussion section.

Table 6-1 – Summary of parameters used to obtain fitted results.

Consistence Parameter	**Gd**	**$Gd_{0.76}Tb_{0.24}$**	**$Gd_{0.85}Er_{0.15}$**
Static Conductivity Adjustment	4	10	0
Curie Temperature (Used/Reference) (K)	295/295	278/278	265/261
Peak MCE (Used/Reference) (K)	5.65/5.65	5.80/5.80	5.00/4.50

6.1.2 No-Load Pressure Variation

Pressure is also an important operating parameter since it affects the density and hence the mass flow rate of the heat transfer fluid. Pressure variation simulations are conducted for single puck Gd regenerators and compared to

experimental results for the same conditions. The results for simulations with no additional losses are shown in Figure 6.4. This plot shows that, for these conditions, a reduction in the simulated system pressure actually results in an increase in temperature span, contrary to the trend observed in the experimental results.

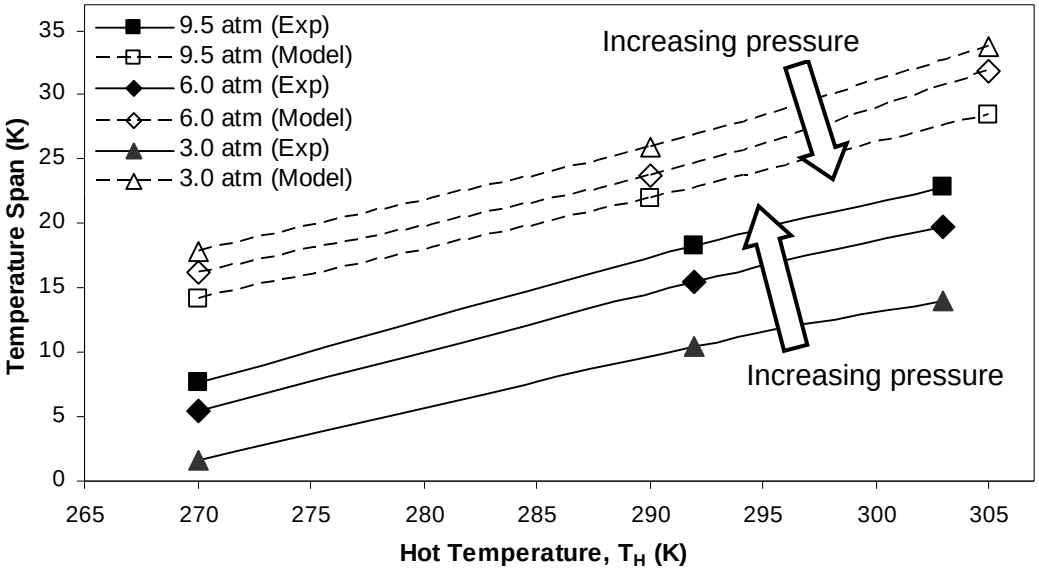

Figure 6.4 – Experimental pressure variation results compared to baseline simulation results for Gd AMRs with an operating frequency of 0.65 Hz.

Figures 6.5 through 6.7 illustrate the effects of systematic application of the adjustments used to generate fitted results with the single puck Gd temperature variation simulations being applied to simulations at 9.5, 6.0, and 3.0 atm, respectively. This process yields model results that are in agreement with experimental data at all three pressures, with deviations up to 1.5 K. However, it is important to note that effect of accounting for radiation is quite different in each of the cases. As shown in Figure 6.5, applying radiation to simulations at 9.5 atm has a small impact on the performance of the regenerators. Conversely, accounting for radiation in the 3.0 atm simulations, as is depicted in Figure 6.7, has a dramatic effect on the temperature span across the AMRs. The effect of this modification on the performance of Gd regenerators operating at 6.0 atm is more moderate, as can be seen in Figure 6.6. Although not shown here, pressure variation simulations are also carried out without any radiative loading.

In this case, it is not possible to obtain simulation results that are in agreement with experimental data across the range of operating pressures being considered by solely adjusting the value of the static conductivity. The significance of these observations is examined in Chapter 8.

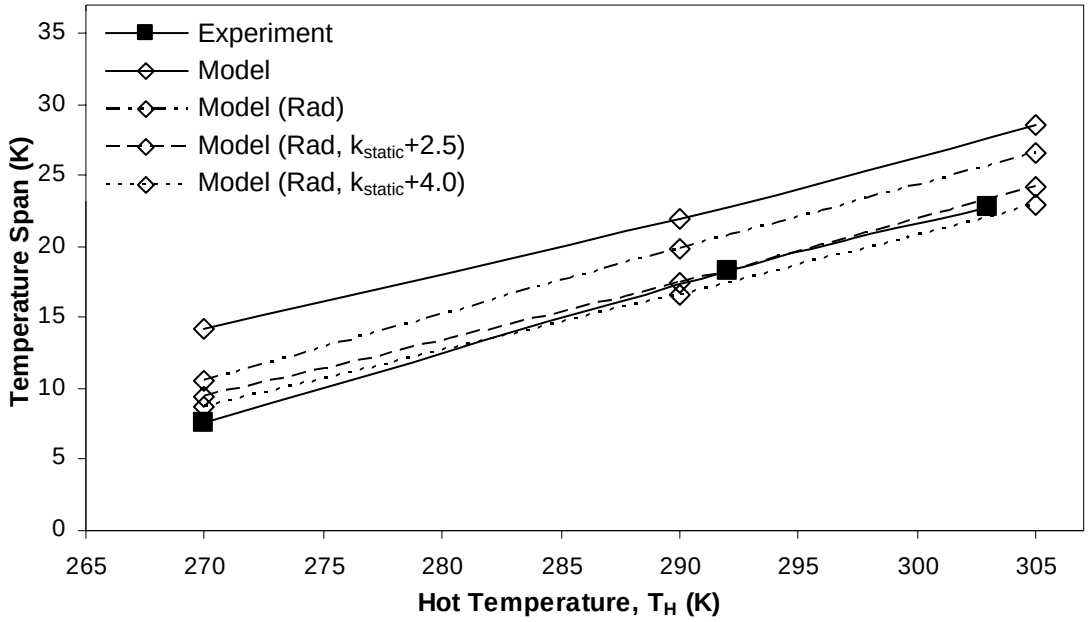

Figure 6.5 – Comparison of results for Gd and a system pressure and frequency of 9.5 atm and 0.65 Hz.

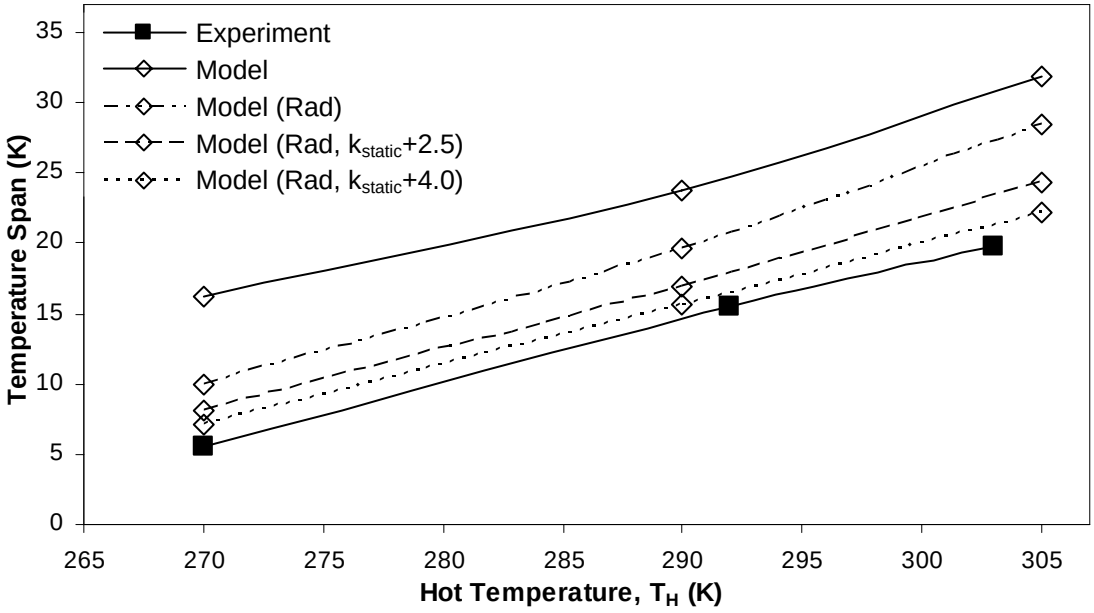

Figure 6.6 – Simulation results compared to experimental results for Gd AMRs, a system pressure of 6.0 atm, and an operating frequency of 0.65 Hz.

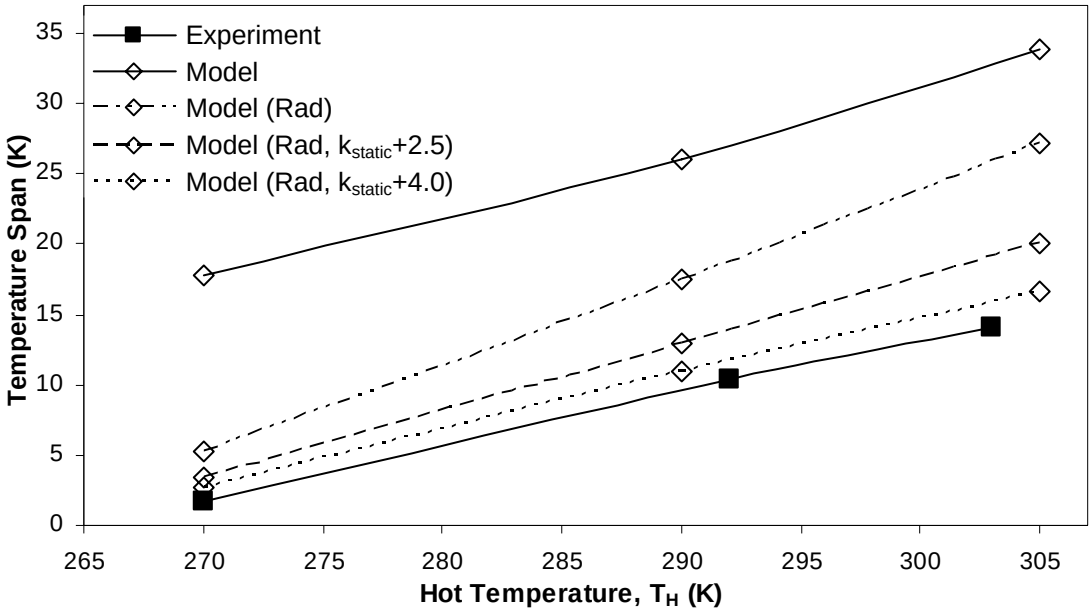

Figure 6.7 – Temperature variation results compared for Gd AMRs operating at 3.0 atm and 0.65 Hz.

6.1.3 Heat Load Application

Simulations are also performed to mimic the application of a heat load in the cold section. These tests are used to represent the operation of the AMRTA with a particular cooling power. It is important to investigate the sensitivity of AMRs with respect to applied heat load because this demonstrates the refrigeration potential of AMR devices. It should be noted, however, that the cooling power of the single puck regenerators being investigated here is relatively small. This is largely due to the small mass of magnetocaloric material used in these components. Figures 6.8 and 6.9 illustrate the results of the Gd heat load simulations in comparison to the results obtained from the AMRTA for system pressures of 9.5 and 4.75 atm, and an operating frequency of 0.80 Hz. Although the magnitudes of some of the temperature spans are found to deviate by up to 2.0 K from the experimental data, the slopes of the curves are in good agreement.

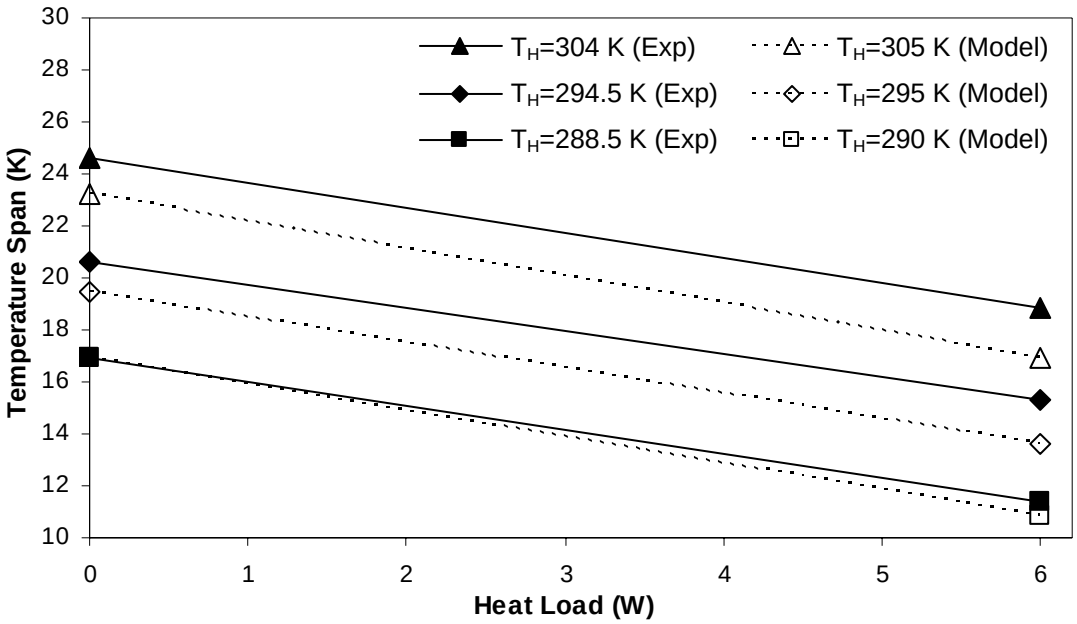

Figure 6.8 – The effect of heat loading on the temperature span of Gd single puck AMRs at a system pressure of 9.5 atm and a frequency of 0.8 Hz.

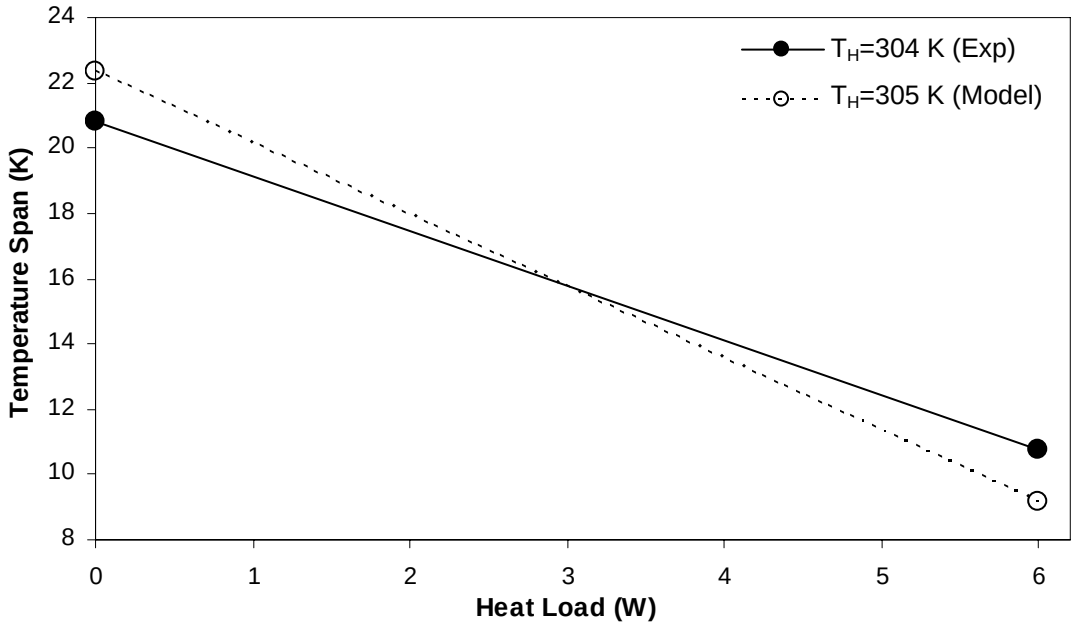

Figure 6.9 – Temperature span as a function of heat load for Gd AMRs, a system pressure of 4.75 atm, and an operating frequency of 0.8Hz.

6.2 Two Puck Simulations

Two puck simulations are also performed using combinations of Gd, $Gd_{0.76}Tb_{0.24}$, and $Gd_{0.85}Er_{0.15}$. The effects of varying hot sink temperature and applied heat load are examined. Loss adjustments that were used in the single puck

simulations to produce simulation results fitted to experimental data, as summarized in Table 6-1, are used in all of the two puck modeling presented in this section. One major difference between the one and two puck experiments is that intermediate temperatures are also measured in the two puck tests, as is shown in Figure 5.3. Thus, the individual contribution of each of the layers can be examined for this set of experiments. The temperature span across each of the pucks is also easily obtained from the two puck simulation results, and so, these results are compared as well.

6.2.1 No-Load Temperature Variation

The effects of varying hot heat sink temperature are examined for simulated two puck Gd-Gd, Gd-$Gd_{0.76}Tb_{0.24}$, and Gd-$Gd_{0.85}Er_{0.15}$ AMRs. The results of these simulations are then compared to experimental results acquired from the AMRTA.

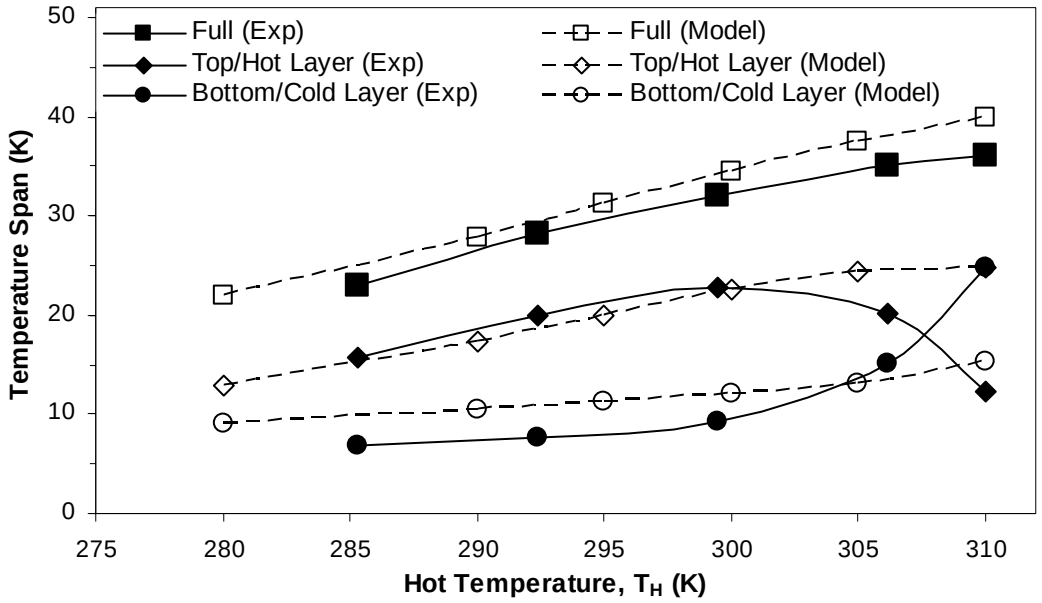

Figure 6.10 – The effect of temperature variation seen both experimentally and with the simulation for Gd-Gd AMRs operating at 9.5 atm and 0.65 Hz.

The results of this analysis for the Gd-Gd are shown in Figure 6.10. The overall temperature span results from the simulation are in good agreement with the experimental data, with a 10% maximum deviation. An investigation of the individual puck contributions yields some interesting results. Up to approximately

300 K, the simulated temperature span of the top regenerator shows less than 1.0 K deviation from the experimental data, while the simulated performance of the bottom layer is consistently overestimated by about 3.0 K. Above 300 K, experimental data shows that the performance of the top layer begins to quickly decline while the temperature spans across the bottom layer begin to quickly increase. These effects are not mirrored in simulated individual layer contributions, with the established trends essentially continuing at hot heat sink temperatures above 300 K. Nevertheless, the overall temperature spans do not show any large deviation from each other in this region, suggesting that the performance increase of the bottom layer is somewhat balanced by the performance decrease of the top layer.

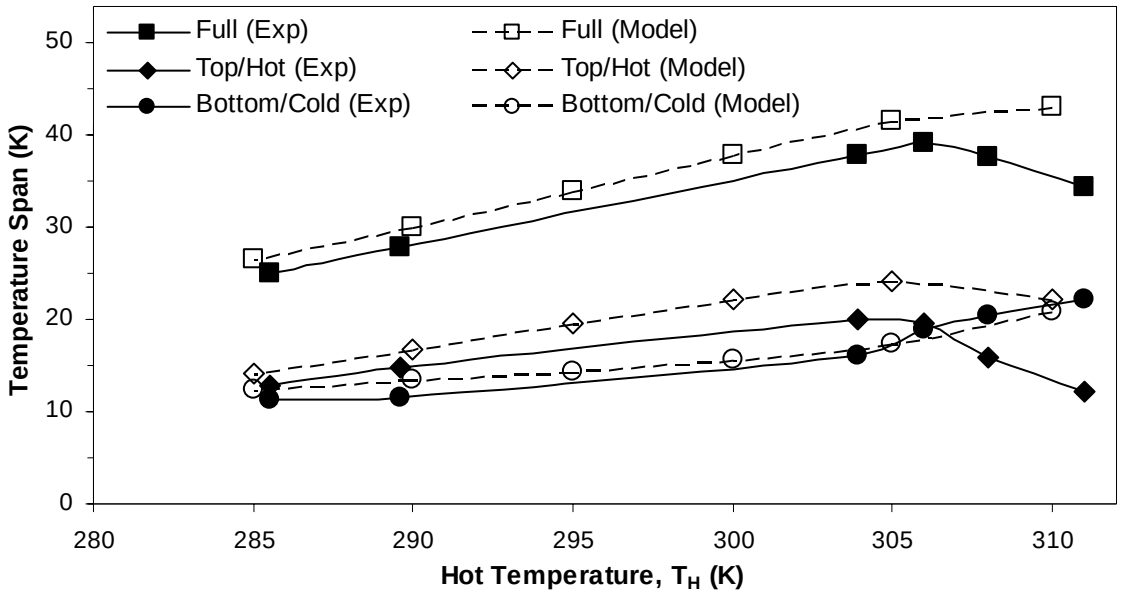

Figure 6.11 – A comparison of experimental and model results for varying hot heat sink temperature with Gd-$Gd_{0.76}Tb_{0.24}$ AMRs at 9.5 atm and 0.65 Hz.

The hot heat sink temperature variation results for the Gd-$Gd_{0.76}Tb_{0.24}$ AMRs are illustrated in Figure 6.11. The magnitude of the overall simulated temperature span deviates from the experimentally obtained data by approximately 10%, except at 310 K, where the variation increases to about 30%. This seems to be due to the fact that the simulations predict that the peak AMR performance occurs at a higher hot sink temperature. As with the Gd-Gd simulations, the experimental data shows sudden changes in the performance of the individual

layers above hot sink temperatures of 305 K. The simulated bottom layer temperature span tracks experimental data well throughout the hot sink temperature range being tested. Conversely, the simulated top layer performance significantly deviates from the experiments and does not follow the sudden temperature span decrease seen experimentally at about 306 K.

Lastly, the hot sink temperature variation results for the Gd-$Gd_{0.85}Er_{0.15}$ AMRs are shown in Figure 6.12. Although the peak temperature spans seem to occur at more consistent hot heat sink temperatures in this case, the simulated overall performance is overestimated by approximately 20% throughout the range being examined. This variation is also present in the comparison of the performance of the individual pucks. However, it is apparent that the simulated temperature span of the top layer is in better agreement with the experimental data than the bottom puck.

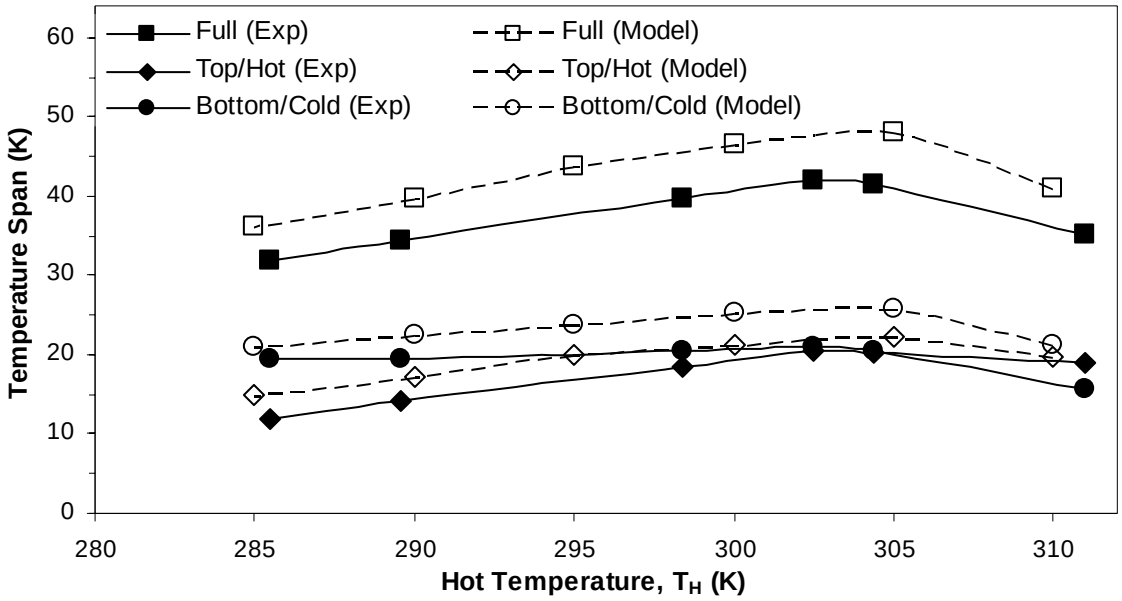

Figure 6.12 – Temperature span as a function of hot heat sink temperature for Gd-$Gd_{0.85}Er_{0.15}$ regenerators operating at 9.5 atm and 0.65 Hz.

6.2.2 Heat Load Application

The effects of varying degrees of applied heat load on the performance of the two puck regenerators are also investigated. Once again, it is possible to compare the temperatures at the interface of the pucks since experimental data

is also obtained for this location. The hot sink temperatures and heat loading ranges used in the simulations are based on the available experimental results.

The results of this analysis for Gd-Gd AMRs are shown in Figure 6.13. The model consistently overestimates the overall performance of the AMRs by approximately 10%. However, investigation of the performance of the individual layers yields an interesting result since the simulation results once again do not follow a cross-over that occurs at approximately 6.5 W of applied heat loading. A similar event was observed in the hot heat sink temperature variation behaviour of the Gd-Gd AMRs, as can be seen in Figure 6.10.

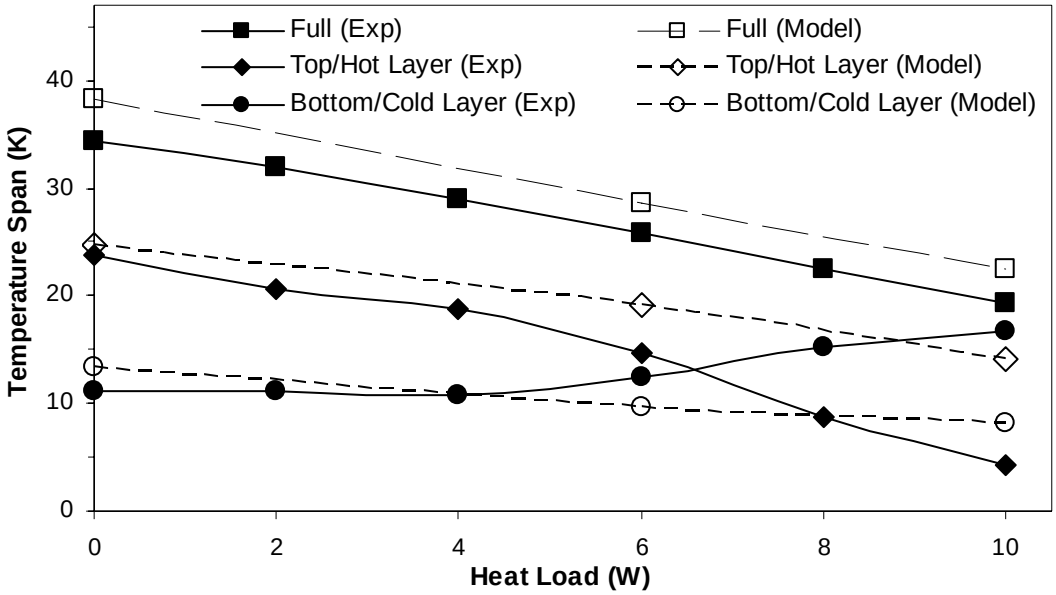

Figure 6.13 – A comparison of simulation (T_H=304 K) and experimental (T_H=305 K) data for the heat load performance of Gd-Gd AMRs operating at 9.5 atm and 0.8 Hz.

Depicted in Figure 6.14, simulated heat load application results are also obtained for Gd-$Gd_{0.76}Tb_{0.24}$. The variation between the overall temperatures spans is found to increase with applied heat load, such that the deviation at 8 W is approximately 25%. The difference between the simulated and experimentally obtained layer performance contributions is also quite large, varying between 10 and 35%.

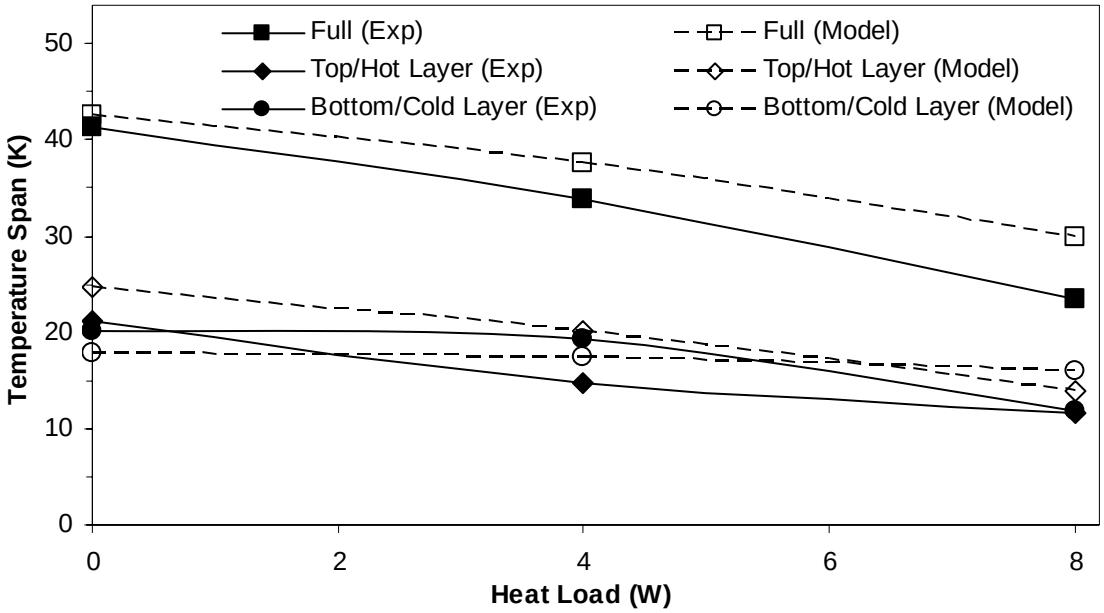

Figure 6.14 – Experimental (T_H=306 K) and model (T_H=305 K) results for the heat load sensitivity of Gd-$Gd_{0.76}Tb_{0.24}$ AMRs operating at 9.5 atm and 0.8 Hz.

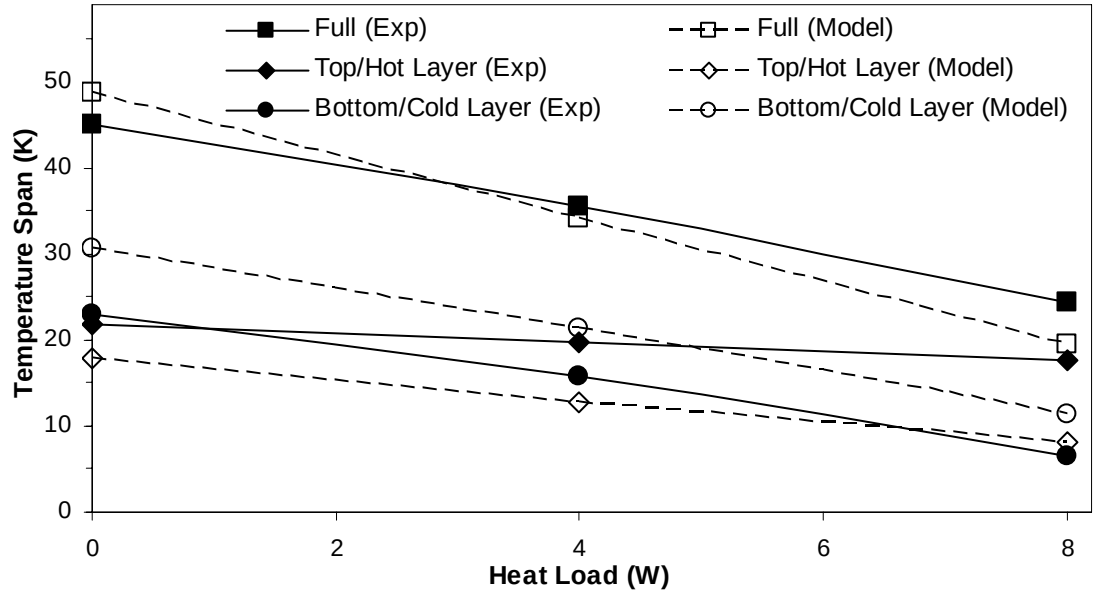

Figure 6.15 – Experimental (T_H=306 K) and model (T_H=305 K) results for heat load sensitivity with Gd-$Gd_{0.85}Er_{0.15}$ regenerators operating at 9.5 atm and 0.8 Hz.

The performance of Gd-$Gd_{0.85}Er_{0.15}$ AMRs with varying applied heat load is investigated at two hot heat sink temperatures. Results for a hot sink temperature of approximately 305 K are shown in Figure 6.15. The overall temperature spans vary by as much as 25% while the individual layer contributions are in very poor agreement with deviations as large as 100%.

However, the results obtained for a hot heat sink temperature of 290 K, as shown in Figure 6.16, are quite different. In this case, the simulated and experimentally obtained results for both overall temperature span and the performance of the individual layers are found to deviate by about 5% at most.

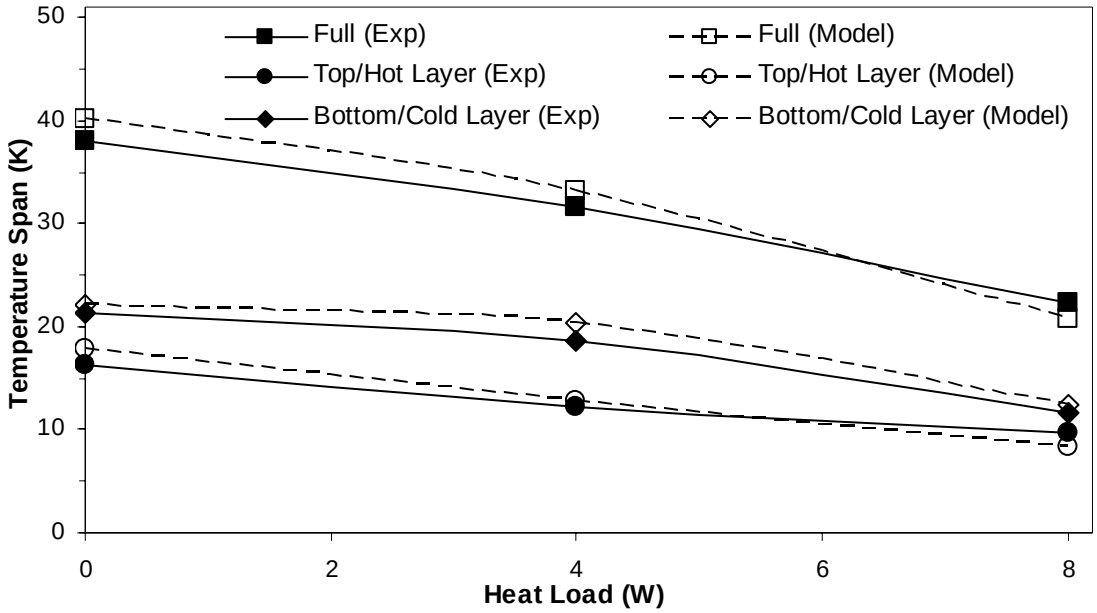

Figure 6.16 – Heat load sensitivity results obtained both experimentally and through simulations (both with T_H=290 K) for Gd-$Gd_{0.85}Er_{0.15}$ AMRs operating at 9.5 atm and 0.65 Hz.

Chapter 7 – Predictive Results

The validation procedure yielded results that are generally in good agreement with experimental data, and so, the simulation is used to predict the performance of the AMRTA in experiments that are either not possible with the current apparatus or have not been conducted thus far. This chapter outlines the results of these predictive simulations. The results are discussed in more detail in Chapter 8.

7.1 Single Puck Simulations

7.1.1 Increased System Pressure

The system pressure is an important operating parameter since it affects the density, and hence the mass flow rate, of the heat transfer fluid. The fluid mass flow rate can have a large impact on AMR performance. This impact can be quantified by consulting the dimensionless parameters defined by Equations (3.13) through (3.17). Taking into account that the heat transfer coefficient is also a function of the mass flow rate, it can be found that NTU is inversely proportional to the mass flow rate ($\propto \dot{m}^{-0.7}$). This parameter is a measure of regenerator effectiveness, and so, this suggests that an AMR will be less effective at higher operating pressures since the thermal mass of the fluid becomes larger in relation to the convective heat transfer occurring between the fluid and the solid. It can also be seen that the utilization parameter, ϕ, defined by Equation (3.14), is proportional to the fluid mass flow rate, and thus the operating pressure. This parameter is a ratio of the fluid and solid thermal masses. It can be sometimes be beneficial to increase the value of the utilization, however, if it is too large, the inlet fluid temperature propagates throughout much of the regenerator. This has a negative impact on the performance of the heat transfer device. What this means with respect to AMRs, is that there is an optimum utilization for peak performance.

Simulations are conducted with single puck Gd AMRs at a system pressure of 15 atm to determine where these regenerators are operating in relation to the

utilization required for peak performance. This pressure is beyond the capabilities of the AMRTA, so it serves as an indicator of whether it would be beneficial to modify the system so that it can operate at higher pressures. As depicted in Figure 7.1, the simulation results, which vary by less than 20% from the experimental data, show that the performance begins to decrease at higher system pressures. This suggests that it may be detrimental to operate at higher system pressures with the single puck AMRs. However, this conclusion cannot be extended to the performance of multi-puck AMRs.

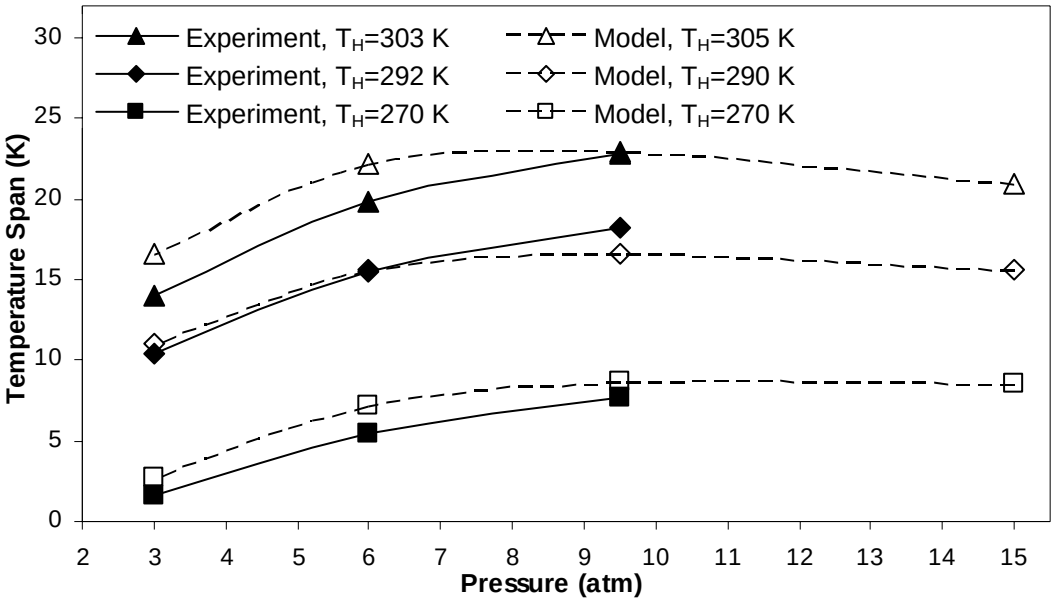

Figure 7.1 – Single puck results for higher system pressure with Gd at 0.65 Hz.

7.1.2 Varying AMR Aspect Ratio

Two major factors must be considered when attempting to optimize the aspect ratio of regenerators. Conductive heat leaks along the length of these porous beds can be reduced by decreasing both their lengths and their cross-sectional areas. However, these modifications result in an increase of the pressure drop across the regenerators. Pressure drop is especially sensitive to cross-sectional flow area. Yet, to reduce the cost of magnetic refrigeration devices, it is important to attempt to limit the diameter of AMRs as much as possible. These cost benefits are largely a result of decreasing magnetic field generator bore diameter.

The choice of aspect ratio for the AMRTA regenerators is somewhat arbitrary, and so, it is interesting to examine the impact of varying this parameter. As depicted in Figure 7.2, this is accomplished by comparing the hot sink temperature variation behaviour of a single Gd AMR puck with aspect ratios of 0.5, 1.0, and 2.0. This indicates that the lengths of the regenerators are either halved or doubled compared to the baseline case, whose results are shown in Section 6.1.1. The diameters of the AMRs in each of the simulations are also adjusted so that a uniform volume of regenerator material can be maintained. Simulation results suggest that the no-load performance of Gd AMRs improves with increasing aspect ratio. This essentially implies that it is more effective for AMRTA regenerators to be longer and thinner. However, it is important to note that, as a result of viscous dissipation being neglected, the varying pressure drop is not accounted for in these simulations. The results of this analysis are discussed in more detail in Chapter 8.

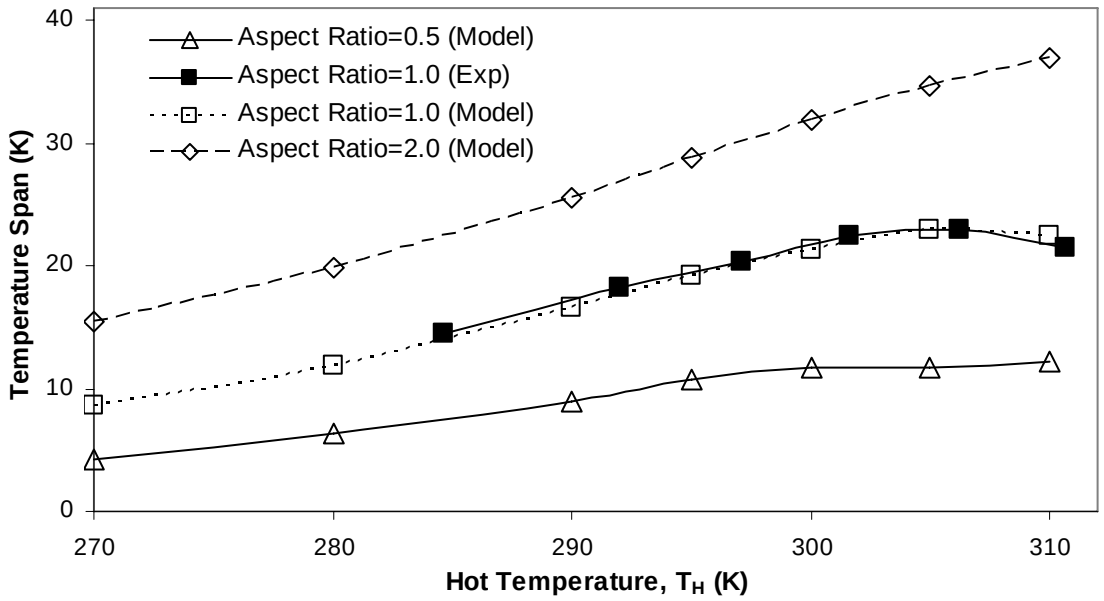

Figure 7.2 – Temperature variation results with Gd AMRs of different aspect ratio, operating at 0.65 Hz and 9.5 atm.

7.2 Two Puck Simulations

7.2.1 Varying Material Proportions

The next set of predictive simulations was centred on the performance of two puck, dual material AMRs with varying material proportions. It has recently been proven experimentally that layering of two or more materials can improve the performance of AMRs [29], however, as of yet, only equal proportions of each material have been used. Although it is intuitive that there are ideal AMR material proportions for each particular set of desired operating conditions, determining the composition of the optimum AMR would be a difficult and time-consuming task if it were to be done experimentally.

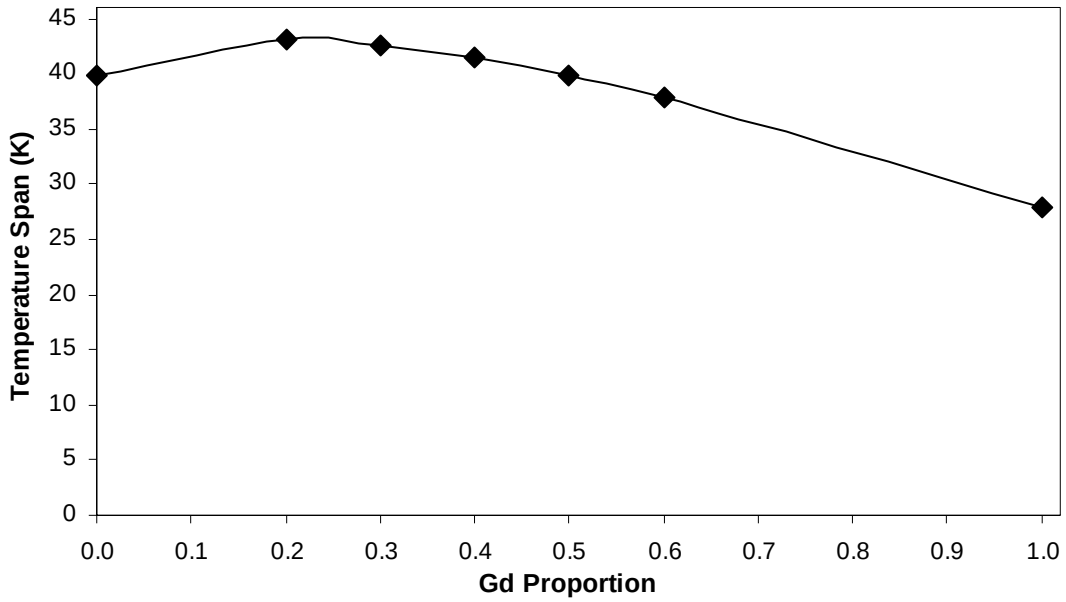

Figure 7.3 – The effect of varying the Gd proportion in a Gd-$Gd_{0.85}Er_{0.15}$ AMR operating at 9.5 atm and 0.65 Hz, and with a hot heat sink temperature of 290 K.

Simulations with varying material proportions are carried out with Gd-$Gd_{0.85}Er_{0.15}$ AMRs and a hot heat sink temperature of 290 K. These parameters are chosen since the heat load simulations at similar conditions, as shown in Figure 6.16, yield results that match experimental data quite well. The results of this analysis, depicted in Figure 7.3, suggest that the optimum regenerator for these conditions is composed approximately of 20% Gd and 80% $Gd_{0.85}Er_{0.15}$.

Although this implies that a regenerator of this composition has improved performance in a no load situation, it is also interesting to examine and compare the performance of this AMR with others as a heat load is applied. This is done to simulate the operation of an AMR refrigerator with a particular cooling power. Figure 7.4 compares the performance of two puck AMRs with varying proportions of Gd and $Gd_{0.85}Er_{0.15}$ as heat loads are applied. From this plot it is clear that the optimum regenerator for the no-load conditions (i.e. 20% Gd) is not as effective in operation with higher heat loads.

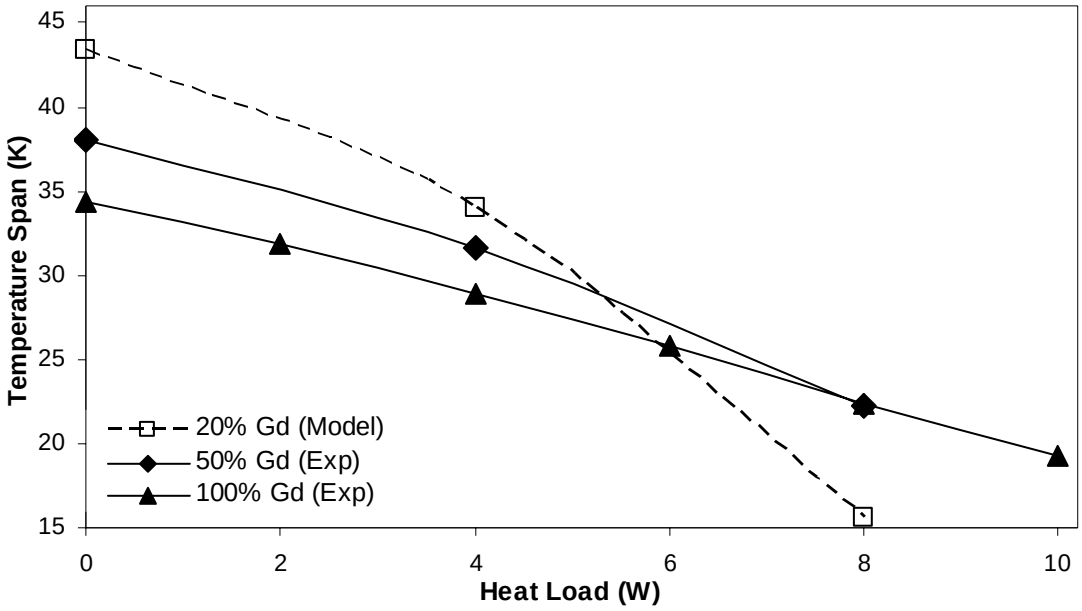

Figure 7.4 – The heat load performance of Gd-$Gd_{0.85}Er_{0.15}$ AMRs with varying proportions of Gd, operating at 9.5 atm and 0.8 Hz.

Chapter 8 – Discussion

This chapter presents an analysis and discussion on the model validation and prediction results that were obtained. Several observations are made that will aid in identifying modifications that can be performed to improve the validity of the simulation.

8.1 Analysis of Model Validation Results

The model was validated by comparing its output to experimental results for variations in hot sink temperature, system pressure, and heat load. The performance of three different materials and various two layer configurations were tested. Baseline simulations with no additional losses yielded improved performance in comparison to the experimental results. Parameters were then adjusted to account for experimental losses, such as heat leaks and eddy currents, which are not yet accounted for in the AMRTA simulations.

8.1.1 Single Puck Simulations

Figure 8.1 provides a summary of the single puck results for hot sink temperature variation. This plot compares data obtained through AMRTA experiments to fitted simulation results. As was noted in Section 6.1.1, the fit to experimental data was most easily obtained with the Gd simulations. Obtaining fitted results with the other materials was more challenging and required that several parameters be adjusted. Some of this discrepancy can be accounted for by noting that Gd is the most well understood magnetocaloric material. Compared to the other materials being investigated, it has been studied in much more detail and there is much less uncertainty in the value of its properties. Thus, there is a greater probability that the reference data obtained for the Gd is valid. This point highlights the importance of possessing accurate material property data in the development of any simulation.

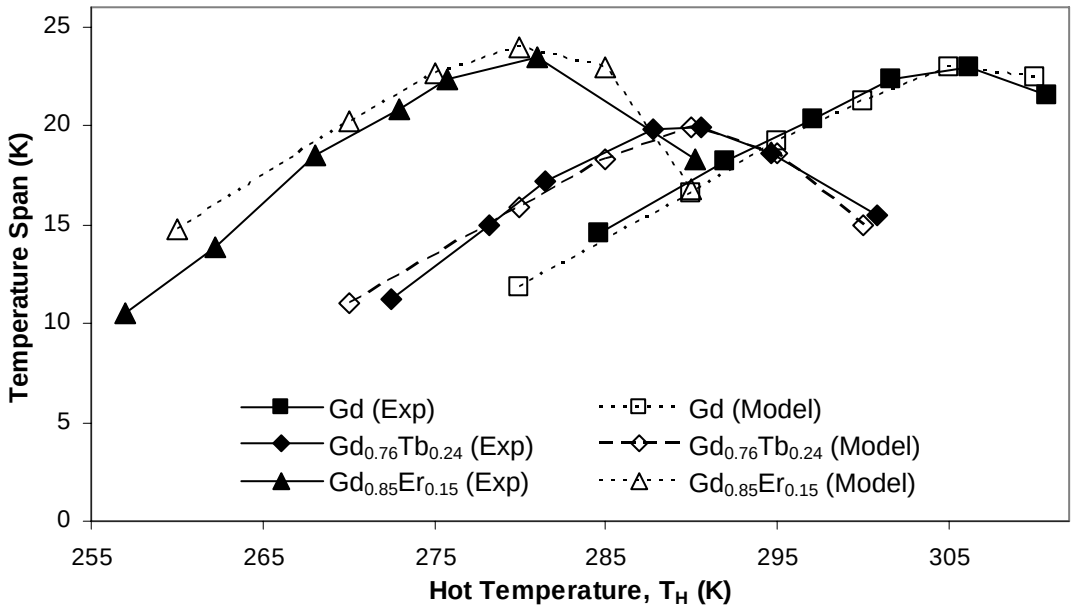

Figure 8.1 – A summary of the hot sink temperature variation behaviour of single puck regenerators operating at 0.65 Hz and 9.5 atm.

Investigating the parameter changes that were required to yield the fitted model results with the different materials also generates some interesting observations. Compared to the Gd, $Gd_{0.76}Tb_{0.24}$ simulations required much larger conductivity, while $Gd_{0.85}Er_{0.15}$ simulations necessitated a decrease in conductivity, a shift in the Curie temperature, and an increase in the maximum MCE used for MCE curve scaling. Therefore, simulation results based on reference values and validation parameters used in the Gd modeling would have yielded a much larger temperature span for $Gd_{0.76}Tb_{0.24}$ and greatly decreased performance for $Gd_{0.85}Er_{0.15}$. Consulting the MCE curve for each of the materials, as shown in Figure 8.2, the peak MCE values for Gd, $Gd_{0.76}Tb_{0.24}$, and $Gd_{0.85}Er_{0.15}$, are 5.65 K, 5.80 K, and 4.50 K, respectively. Based solely on the peak MCE values, it is expected that an AMR composed of $Gd_{0.76}Tb_{0.24}$ would have the best performance while a $Gd_{0.85}Er_{0.15}$ AMR would generate the lowest no-load temperature span. This is contrary to the observed experimental results.

In justification of these experimental results, it has been argued that material heat capacity, as shown in Figure 8.2, also has a large impact on the performance of an AMR [29]. The comparatively low heat capacity of the $Gd_{0.85}Er_{0.15}$, for

instance, may explain the unexpected performance of this material. Model results suggest that either some the reference material data obtained is not valid for the materials being tested or that some physical effects are not properly being accounted for in the AMRTA simulations. For example, it has been noted that the rapid magnetic field changes required by AMR devices may not allow for magnetic transformations to go to completion in materials with slower magnetic ordering times [30]. However, this is not expected to be a concern for the second order materials currently being tested since they have very fast relaxation times. Further analysis is required in order to shed more light on this issue.

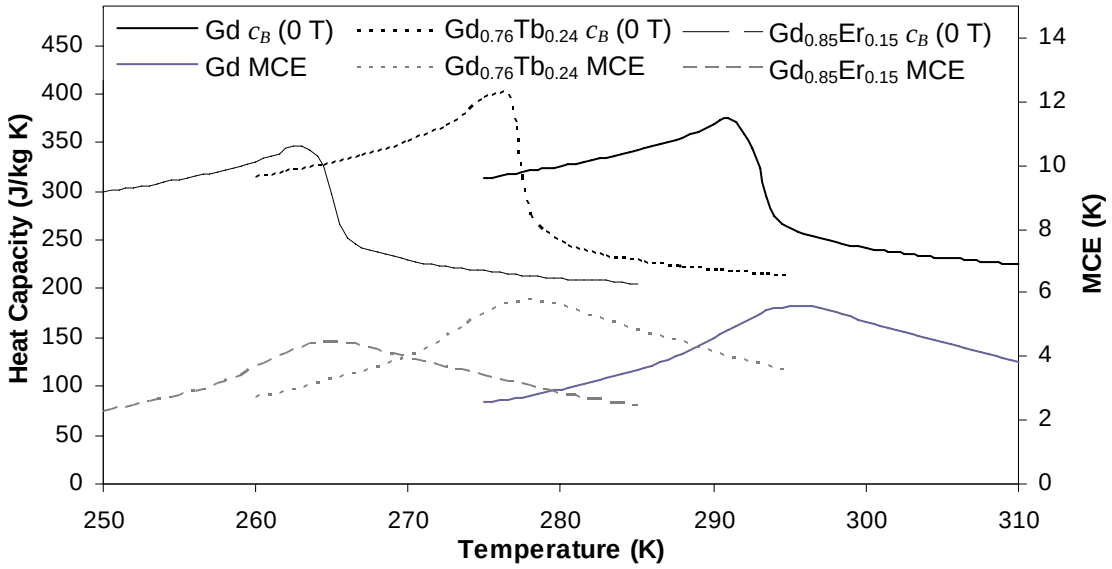

Figure 8.2 – The heat capacity and MCE behaviour of the materials used in the AMRTA experiments and simulations [10, 24].

Although not summarized in a plot here, it is important to note that the model results for Gd were also validated for varying system pressure and heat load. However, as was stated in the Section 6.1.2, it was necessary to apply a radiative load to the cold section in order to obtain simulation results that fit the experimental data with the varying pressure simulations. This is an intuitive result since the performance of an AMR operating at a lower pressure, and thus with a lower utilization, should be more sensitive to heat loading [29]. Obtaining model results that were in agreement with experimental data in all cases that were simulated is encouraging since it suggests that the simulation is applicable

across a wide range of varying parameters. However, it should be noted that this was an iterative process since the same losses were used in all the simulations in order to be consistent.

8.1.2 Two Puck Simulations

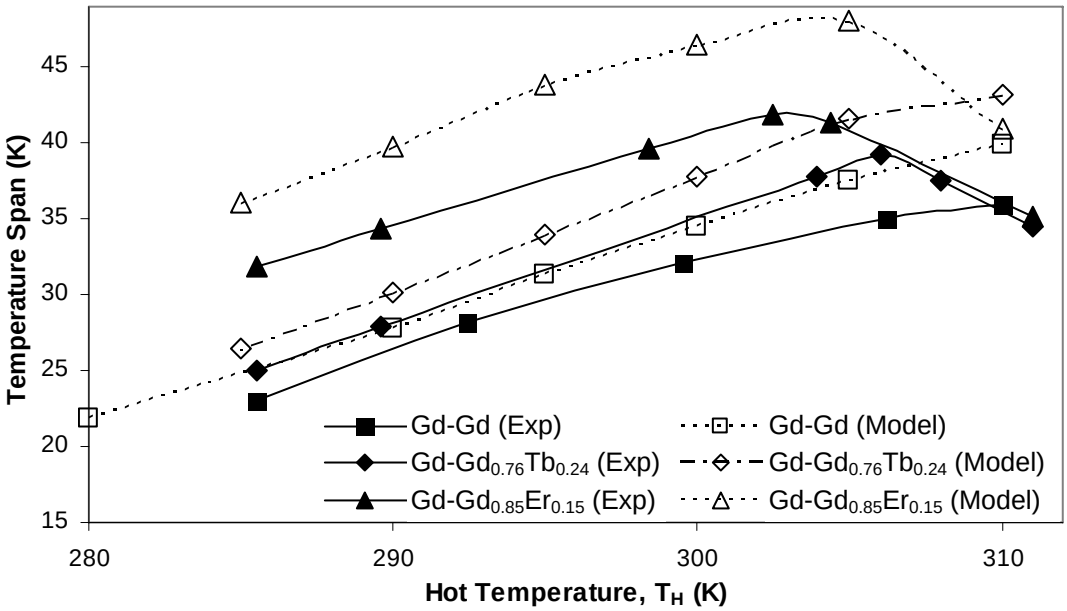

Figure 8.3 – A summary of two puck hot sink temperature variation results at 9.5 atm and 0.65 Hz. Note that, to improve clarity, the vertical axis is not shown to full scale.

Results obtained both experimentally and through simulations for two puck hot heat sink temperature variation are compared in Figure 8.3. As is noted in the results section, the same loss adjustments that helped yield fitted results in the single puck simulations were used for the dual puck modeling. In this case, the modeling results were found to overestimate the performance of the two puck regenerators. This suggests that there may be some mechanisms that are not being accounted for in the simulations. The most obvious of these is viscous dissipation. This is essentially a larger degree of energy dissipation as a result of a longer AMR aspect ratio causing an increased pressure drop. It was initially thought that losses due to viscous dissipation could be accounted for through other loss mechanisms and that the change in its magnitude would be negligible between tests. However, these results suggest that viscous dissipation should be accounted for in future simulations.

Observing the individual contributions of each of the layers in the two puck simulations, as with the Gd-Gd results depicted in Figure 8.4, also yields an interesting result. At hot heat sink temperatures significantly above the Curie temperature of approximately 295 K for Gd, a sudden change is seen in the experimental performance of each layer. The cold layer, which had contributed to a lesser degree until this point, begins a drastic improvement in its performance and vice-versa. In fact, the curves indicating the relative contribution of each layer were found to cross each other in this vicinity. This effect was not seen in the simulations yet the total simulated temperature span in this region was found to be similar to experiments.

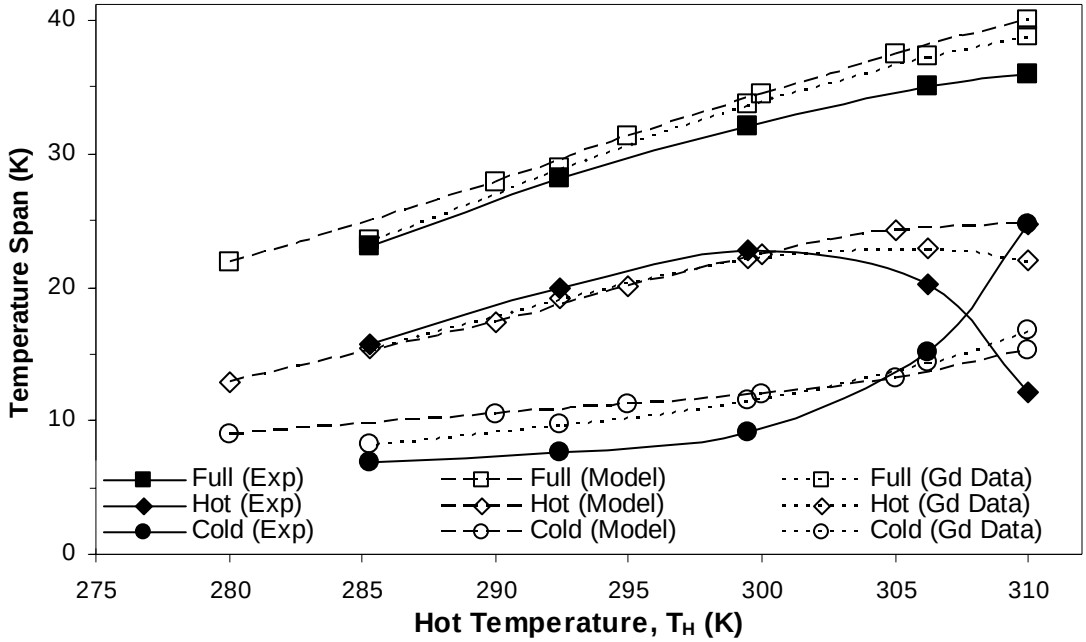

Figure 8.4 – Experimental, model, and predictive [29] results for the temperature variation behaviour of Gd-Gd AMRs operating at 9.5 atm and 0.65 Hz.

It is instructive to compare these results to predictive results for the performance of the Gd-Gd AMRs [29]. These results were generated using experimental findings for the single layer performance of Gd regenerators. The temperature span of the top or hot layer was estimated by direct use of the data. This yielded an intermediate temperature so that the temperature span of the bottom, or cold layer, and thus the total temperature span, could then be approximated. In some cases, it was necessary to extrapolate the performance of the bottom layer since

experimental results were not available at this particular hot sink temperature. The results of this analysis, also depicted in Figure 8.4 and labelled as Gd data, are remarkably similar to the simulated results. Once again, the overall temperature span is fairly consistent with the experimental results but the individual layer contributions at hot sink temperatures above the Curie temperature do not exhibit the crossing in performance seen with the experimental data.

This discrepancy may be a result of a magnetic interaction that is not accounted for in either of the simulated cases. At hot sink temperatures significantly above the Curie temperature of the material, a portion of the hot layer of the AMR is paramagnetic while the rest is ferromagnetic. The ferromagnetic portion of the hot layer improves the performance of the bottom layer by helping to channel the magnetic field lines in this area. The magnetic field lines would otherwise begin to diverge and diminish the performance of the bottom layer. This consequence is referred to as demagnetization and the ferromagnetic portion of the top layer is said to be a “magnetic flux shim” for the bottom layer [31]. Magnetic interactions can become considerably more complex in regenerators composed of multiple materials.

8.2 Analysis of Predictive Results

The predictive results are useful in briefly demonstrating the potential that an experimentally validated simulation has to become a vital tool in a parallel program of AMR research through both experiments and numerical simulations. For instance, the increased pressure simulations are useful in substantiating the claim that increasing the operating pressure of the AMR test apparatus will only yield marginal improvements in the performance of single puck regenerators. Testing this experimentally would require that components rated for higher pressures be installed on the apparatus.

The varying aspect ratio simulations are also effective in confirming that a performance enhancement can be realized if regenerators with a longer aspect

ratio are used. This is due to a decrease in the conduction loss across these regenerators. However, it is believed that the magnitude of the predicted improvement, as shown in Figure 7.2, is overestimated. This assumption is due to the fact that the losses due to viscous dissipation in regenerators with longer aspect ratios are not properly accounted for in the simulations thus far.

The two puck simulations with varying material proportions, depicted in Figure 7.3, potentially represent one of the most important applications of the AMRTA simulation. The capability to predict the optimum composition of a multi-layered regenerator for operation with a particular set of operating parameters would be vital to the successful commercialization of a magnetic refrigeration device. Although it has been proven that multi-material AMRs have the potential to improve the performance of magnetic refrigeration systems, it has been noted, both in this and in other analyses [29], that the performance of the multi-material regenerators tends to be more sensitive to heat loading. Shown in Figure 7.4, the last set of predictive simulations for varying heat load with Gd-$Gd_{0.85}Er_{0.15}$ AMRs highlights this point and the importance of optimizing the composition of regenerators for the particular set of operating conditions.

Chapter 9 – Conclusions and Recommendations

A great deal of research must be conducted before AMR refrigeration becomes commercially viable, either for room temperature refrigeration applications or for the liquefaction of natural gas and hydrogen. The purpose of this research is to help address the optimization of parameters such as system mass flow rate and frequency, and AMR shape, aspect ratio, and material composition through the development of a model that can accurately simulate the operation of the AMRTA. This allows for a parallel program of research through numerical simulation and experimentation to occur.

In order to accomplish this it was necessary to develop a set of governing equations that would accurately describe the flow of energy through the system. Material data and property correlations were obtained so that the simulation could be integrated into a finite element modeling package. The most important step was to then validate the model output by comparing model data with experimental results that had been obtained for the same set of operating parameters. Lastly, some predictive simulations were carried out to showcase the applicability of an accurate AMR refrigeration cycle model.

The model that was developed has a number of advantages over previous simulations. For instance, the model domain encompasses two AMRs and the cold section in between them. This allows for a more accurate representation of the AMR test apparatus since only one boundary condition, the hot heat sink temperature, needs to be specified. Further, a realistic model of the AMRTA magnetic refrigeration cycle with magnetic field and mass flow rate variations occurring simultaneously and varying in a sinusoidal manner is implemented in this work. The most important difference between this work and previous models, though, is the existence of experimental data with which to confirm its accuracy. This resource allows for the simulation to be incrementally refined and yield a more accurate representation of the physical test apparatus.

Simulation results that are in agreement with experimental data were obtained with single puck regenerators, however, this was more difficult to accomplish with materials other than Gd. It is recommended that efforts be made to obtain more accurate material property data for the materials being tested, perhaps through analyzing the very same material that is used in experiments. Modeling results for two puck regenerators with the same losses used to produce consistent results in single-puck tests yielded overestimates of AMR performance. To address this concern, it is recommended that viscous dissipation be incorporated into the simulation. Further, it is recommended that a more thorough validation procedure be carried out to determine the adjustments that are most successful at replicating experimental results over a broad range of operating conditions. Lastly, demagnetizing effects should be incorporated into the simulation to address inconsistencies that were found between the simulated and experimental results for the individual puck contributions in two puck regenerators. These modifications will allow for the potential of this powerful AMRTA model to be realized.

References

[1] Hydrogen Systems: A Discussion Paper for Greenhouse Gas Reduction and Economic Growth, CHA Discussion Paper, May 15, 2005.

[2] Miller, A., “Constraining Climate Change with Nuclear Electricity and Hydrogen (N + H2),” AECL Report 12142, 2003.

[3] Ritter, J. A., Ebner, A. D., Wang, J., Zidan, R., “Implementing a Hydrogen Economy,” Materials Today, pp. 18-23, Sept. 2003.

[4] Schrope, M., “Which Way to Energy Utopia?,” Nature, vol. 414, pp. 682-684, Dec. 13, 2001.

[5] T-Raissi, A., Hesselmann, K., Funk, J. E., “Exergy Analysis of Hydrogen Liquefaction Cycles,” Proceedings of 18th International Congress of Refrigeration, Paper No. 526, 1991.

[6] Pecharsky, V. K., Gschneidner, K. A., “Magnetic Refrigeration,” Intermetallic Compounds: Principles and Practice, vol. 3, pp. 519-539, 2002.

[7] Pecharsky, V. K., Gschneidner, K. A., “Magnetocaloric Effect and Magnetic Refrigeration,” Journal of Magnetism and Magnetic Materials, vol. 200, pp. 44-56, 1999.

[8] Nave, R., “Ferromagnetism,” http://hyperphysics.phy-astr.gsu.edu/hbase/solids/ferro.html, 2004.

[9] Richard, M. A., Rowe, A., Chahine, R., “Magnetic Refrigeration: Single and Multimaterial Active Magnetic Regenerator Experiments,” Journal of Applied Physics, vol. 95, no. 4, pp. 2146-2150, 2004.

[10] Dan’kov, S. Y., Tishin, A. M., “Magnetic Phase Transitions and the Magnetothermal Properties of Gadolinium,” Physical Review B, vol. 57, no. 6, pp. 3478-3490, 1998.

[11] Rowe, A.M., “Active Magnetic Regenerators: Performance in the Vicinity of Para-ferromagnetic Second Order Phase Transitions,” Ph.D. Thesis, University of Victoria, 2002.

[12] Richard, M-A., Rowe, A.M., Chahine, R., Bose, T., Barclay. J.A., “Towards Magnetic Liquefaction of Hydrogen: Experiments with an Active Magnetic Regenerator Test Apparatus,” Canadian Hydrogen and Fuel Cell Conference, Vancouver, 2003.

[13] Spearing, I., “A Numerical Model for a Rotary Active Magnetic Regenerative Refrigerator,” M.A.Sc. Thesis, University of Victoria, 1994.

[14] Engelbrecht, K., Nellis, G. and Klein, S., “A Numerical Model of an Active Magnetic Regenerator Refrigeration System,” Air-Conditioning and Refrigeration Technology Institute, 2005.

[15] Smaïli, A., Chahine, R., “Thermodynamic Investigations of Optimum Magnetic Regenerators,” Cryogenics, vol. 38, pp. 247-252, 1998.

[16] Carpetis, C., “An Assessment of the Efficiency and Refrigeration Power of Magnetic Refrigerators with Ferromagnetic Refrigerants,” Advances in Cryogenic Engineering, vol. 39, pp. 1407-1415, 1994.

[17] DeGregoria, A.J., “Modeling the Active Magnetic Regenerator,” Advances in Cryogenic Engineering, vol. 37B, pp. 867-873, 1992.

[18] Matsumoto, K., Hashimoto, T., “Thermodynamic Analysis of Magnetically Active Regenerator from 30 to 70 K with a Brayton-like Cycle,” Cryogenics, vol. 30, pp. 840-845, 1990.

[19] Bejan, A., “Convection Heat Transfer,” John Wiley and Sons, Inc., New York, pp. 2-15, 1995.

[20] “Thermophysical Properties of Fluid Systems,” http://webbook.nist.gov/chemistry/fluid/, 2005.

[21] Barron, R. F., “Cryogenic Heat Transfer,” Taylor and Francis Group, New York, pp. 327-329, 1999.

[22] Caudle, K. J., “Characterization of Regenerator Geometries through Modelling and Experimentation,” M.A.Sc. Thesis, University of Victoria, pp. 17-20, 1997.

[23] Kaviany, M., “Principles of Heat Transfer in Porous Media,” Springer-Verlag Inc., New York, pp. 115-126, 357-369, 1991.

[24] Pecharsky, V. K., Gschneidner Jr., K. A., Ames Laboratory, Iowa State University, private communications, Aug.–Sept. 2005.

[25] “Gadolinium,” http://en.wikipedia.org/wiki/Gadolinium , 2005

[26] Incropera, F. P., DeWitt, D. P., “Introduction to Heat Transfer,” 4th Edition, John Wiley and Sons, New York, pp. 453-464, 769, 2002.

[27] “Cryogenic Technologies Group, Material Properties: G10-CR,” http://cryogenics.nist.gov/NewFiles/G10_CR.html, 2005.

[28] “Thermal and Mechanical Properties of G-10CR,” http://www.yutopian.com/Yuan/prop/G10.html, 2005.

[29] Tura, A., “Active Magnetic Regenerator Experimental Optimization,” M.A.Sc. Thesis, Universiy of Victoria, 2005.

[30] Pecharsky, V.K. and Gschneidner Jr., K.A., “Recent Developments in Magnetocaloric Materials,” Rep. Prog. Phys., vol. 68, pp. 1479–1539, 2005.

[31] Peksoy, O., Rowe, A., “Demagnetizing effects in active magnetic regenerators,” Journal of Magnetism and Magnetic Materials, vol. 288, pp. 424–432, 2005.